



저작자표시-비영리-변경금지 2.0 대한민국

이용자는 아래의 조건을 따르는 경우에 한하여 자유롭게

- 이 저작물을 복제, 배포, 전송, 전시, 공연 및 방송할 수 있습니다.

다음과 같은 조건을 따라야 합니다:



저작자표시. 귀하는 원저작자를 표시하여야 합니다.



비영리. 귀하는 이 저작물을 영리 목적으로 이용할 수 없습니다.



변경금지. 귀하는 이 저작물을 개작, 변형 또는 가공할 수 없습니다.

- 귀하는, 이 저작물의 재이용이나 배포의 경우, 이 저작물에 적용된 이용허락조건을 명확하게 나타내어야 합니다.
- 저작권자로부터 별도의 허가를 받으면 이러한 조건들은 적용되지 않습니다.

저작권법에 따른 이용자의 권리는 위의 내용에 의하여 영향을 받지 않습니다.

이것은 [이용허락규약\(Legal Code\)](#)을 이해하기 쉽게 요약한 것입니다.

[Disclaimer](#)

공학박사 학위 논문

Development of a Single Spark Discharger
for Highly Efficient Nanoparticle Generation

내부 나노입자 생산량 향상을 위한 단일 스파크 방전
장치 개선 연구

2017년 2월

서울대학교 대학원

기계항공공학부

노승렬

Development of a Single Spark Discharger for Highly Efficient Nanoparticle Generation

Seung Ryul Noh

Department of Mechanical and Aerospace Engineering

The Graduate School

Seoul National University

Nanoparticles have been widely used in various applications due to their novel catalytic, optical and electrical properties. Especially, charged aerosol nanoparticles can be utilized in electrostatically controlled deposition techniques. Spark discharge nanoparticle generation is a proper method for generation of charged aerosol nanoparticles at atmospheric and room temperature conditions. However, aerosol particles generated by spark discharge methods generally have a Gaussian charge distribution centered at zero, and these charges come from the plasma between the electrodes as well as the ions generated during the process. Neutralizing and recharging the particles at spark discharge operation lead to low yield of supply of building blocks for electrostatic field assisted lithography. Moreover, scaling up the production capacity of spark discharge generated nanoparticles is crucial for their industrial applications.

Therefore, in this study, we have devised a new strategy to increase the yield of

positively charged nanoparticles, by continuously providing additional positive ions to charge the generated particles *in situ*, using the electrodes as the ion source. We have developed a new spark control circuit that rapidly restores the electrode voltage to values above the corona discharge voltage after spark discharge events. We confirmed 1.8-fold increase in the amount of positively charged particles generated when the new circuit was implemented with pin-to-plate type electrodes.

In addition, for scaling up the production rate of nanoparticles, we have presented a novel wire-to-plate electrode configuration and perform a comparative study between rod-to-rod, wire-to-rod and wire-to-plate spark dischargers to understand the factors affecting stability of spark discharges at high frequencies. The spark duration was found to be inversely correlated with the maximum stable spark frequency, and electric field intensity and carrier gas velocity were identified as two potential parameters that affect the spark stability. And we confirmed that the wire-to-plate electrode configuration has advantages in both aspects, of which geometry allows faster local gas velocity for a given carrier gas flow rate and more intense electric fields for a given electrode voltage. By using wire-to-plate type electrodes, the maximum stable spark frequency of 17.9 kHz and mass production rate of the nanoparticles which was proportional linearly to the spark frequency could be achieved.

Lastly, we have designed a wire-to-cylinder type spark discharger for long-term consistent nanoparticle generation at high frequency regime. We have investigated a proper wall thickness of a cylinder electrode according to electric field simulation with COMSOL program and erosion pattern size of electrodes by spark discharge operation. And we obtained nanoparticle generation with consistent size

distribution during 14 hours of spark discharge operation with different frequencies.

**Spark discharge; charged aerosol; nanoparticle; spark plasma;
high frequency;**

Student Number: 2010-20672

Contents

Abstract	1
Contents	4
List of Figures	8
Chapter 1. Introduction	13
1.1. Background and Objectives of Research	14
Chapter 2. A Spark Discharger Circuit for Generating Positively Charged Nanoparticles	17
2.1. Introduction	18
2.2. Experimental setup	20
2.2.1. Spark control circuit	20
2.2.2. Spark discharger	22
2.2.3. Particle size and charge measurement system	23
2.3. Results and discussion	25
2.3.1. Modified spark control circuit	25

2.3.2. Charge measurement from modified spark discharge system.....	28
2.3.3. Size distribution of charged particles	31
2.3.4. Effects of electrode geometry	34
2.3.5. Effects of flow rate	36
2.4. Conclusion	38

Chapter 3. A Study of Spark Dischargers for Stability

Control in High Frequency Region	40
3.1. Introduction	41
3.2. Experimental setup	43
3.2.1. Three electrode geometries of spark dischargers	43
3.2.2. Spark discharge and Measurement system	45
3.3. Results and discussion	48
3.3.1. Unstable state of spark discharge with Rod-to-Rod electrodes ...	48
3.3.2. Spark duration time analysis	51
3.3.3. Electrical effects on the spark duration time	53
3.3.4. Flow rate effects on the stability of spark discharge	55

3.3.5. Mass production rate analysis	57
3.3.6. High frequency spark discharges with Wire-to-Plate	
Electrodes	59
3.4. Conclusion	62
Chapter 4. Wire-to-Cylinder Type Spark Discharger for	
Long Time Consistent Nanoparticle Generation	63
4.1. Introduction	64
4.2. Experimental setup	66
4.2.1. wire-to-cylinder type electrode spark discharge nanoparticle	
generation system	66
4.2.2. Measurement system	68
4.3. Results and discussion	69
4.3.1. Consideration of cylinder wall thickness	69
4.3.2. Electric field analysis for sustainable spark discharge	72
4.3.3. Durability enhancement of Wire-to-cylinder type electrode	78
4.4. Conclusion	81

Chapter 5. Concluding Remarks	82
Acknowledgement	85
References	86
국문 초록	92

List of Figures

Figure 2.1. (a) Conventional spark control circuit and (b) the modified spark control circuit implemented in this study.

Figure 2.2. Schematic of the experimental setup consisting of spark control circuit, spark discharge chamber (showing pin-to-plate electrodes), and particle number and charge measurement system.

Figure 2.3. (a) A typical saw tooth voltage profile obtained from conventional spark control circuit. (b) Truncated saw tooth voltage profiles at the electrodes where it recovers quickly to the set voltage on the additional high voltage power supply (HVPS2) after a spark discharge event.

Figure 2.4. (a) Total current measured by the Faraday cup electrometer directly from the outlet of spark discharger with $V_2 = 3400$ V. (b) The current from charged particles only measured by Faraday cup electrometer after DMA filtering at various V_2 voltages.

Figure 2.5. Charged particle size distributions obtained by using the modified spark control circuit at $V_2 = 3400$ V.

Figure 2.6. (a) Positively charged particle size distributions, and (b) negatively charged particle size distributions obtained by using the modified spark control circuit with various V2 values.

Figure 2.7. Particle size distributions obtained by using the new spark control circuit with various electrode configurations; (a) rod-to-plate and (b) wire-in-hole configuration.

Figure 2.8. The effect of carrier gas flow rate on positively charged particle size distributions with pin-to-plate configuration. The positive particle yield enhancement diminishes at high flow rates.

Figure 3.1. Three different electrode configurations (a) rod-to-rod, (b) rod-to-plate and (c) wire-to-plate. Blue arrows indicate carrier gas inflow

Figure 3.2. Schematics of experimental setup showing wire-to-plate electrode configuration as an example.

Figure 3.3. Voltage profiles from rod-to-rod electrode type spark discharger. (a) Frequency of 1.1 kHz. (b) Frequency of 3.7 kHz; unstable state with discharge voltages below the desired breakdown voltage (2.2 kV)

Figure 3.4. Current and voltage profiles during spark discharge events at 1 kHz spark frequency. (a) rod-to-rod, (b) wire-to-rod, and (c) wire-to-plate electrode configuration.

Figure 3.5. (a) Spark duration time of wire-to-plate electrode type spark discharger as spark frequency increases (Capacitance 1nF, breakdown voltage 2.2 kV, N₂ flow rate 6.7 lpm. (b) Voltage profiles during spark discharge events at 1.1 kHz and 17.9 kHz.

Figure 3.6. Voltage profiles from wire-to-plate electrode type spark discharger with frequency of 14 kHz with carrier gas (N₂) flow rates of (a) 4.1 lpm and (b) 6.7 lpm.

Figure. 3.7. Mass production rate of nanoparticles (Cu) scale linearly with (a) spark frequency (Capacitance 2 nF), up to the maximum stable spark frequency, and (b) external capacitance, at spark frequency of 10 kHz and flow rate of 6.7 lpm.

Figure 3.8. Voltage profiles from wire-to-plate electrode type spark discharger at different frequency: (a) 4.5 kHz, (b) 9.1 kHz and (c) 17.9 kHz.

Figure 3.9. TEM images of agglomerated copper nanoparticles generated at (a) 4.5 kHz, (b) 9.1 kHz, and (c) 17.9 kHz. (d) Size distribution of generated nanoparticles

at each frequency showing increasing geometric mean diameter and total number concentration as the frequency increases. The energy per spark and the gas (N₂) flow rate are 4.84 mJ and 6.7 lpm in all the cases.

Figure 4.1. Schematic of spark discharge nanoparticle generation system which consist of external circuit and spark discharge chamber (blue arrow indicate carrier gas inflow)

Figure 4.2. Optical images of spark electrode front surface (rod type) after spark discharge erosion. (Adopted from M. Wagner et al. 2016)

Figure 4.3. Confocal laser scanning height maps of patterns found on Ni electrode front surfaces of initially cathodic (a) and anodic polarity after spark discharge erosion. (Adopted from M. Wagner et al. 2016)

Figure 4.4. The COMSOL modelling of inner volume of spark discharge chamber with wire-to-cylinder type electrode (1mm diameter of wire, 0.2 mm thickness of cylinder wall case)

Figure 4.5. (a) Electric potential between electrodes (upper) and electric field normalization value along the path 1 and 2 when using the cylinder wall thickness

of 1 mm.

Figure 4.5. (b) Electric potential between electrodes (upper) and electric field normalization value along the path 1 and 2 when using the cylinder wall thickness of 0.5 mm.

Figure 4.5. (c) Electric potential between electrodes (upper) and electric field normalization value along the path 1 and 2 when using the cylinder wall thickness of 0.2 mm.

Figure 4.6. Long-term stability of nanoparticle size distribution with frequency of (a) 1.5 kHz (b) 3 kHz (c) 5 kHz by using wire (1mm diameter) -to-cylinder (1.6 mm inner diameter, 0.2 mm thickness) type electrode spark discharger.

Figure 4.7. Long-term stability of (a) geometric mean diameter, (b) total number concentration and (c) geometric standard deviation with different frequencies by using wire (1mm diameter) -to-cylinder (1.6 mm inner diameter, 0.2 mm thickness) type electrode spark discharger.

Chapter 1.

Introduction

1.1. Background and Objectives of Research

Spark discharge generation (Schwyn et al. 1988) is a simple, clean and energy efficient method which is performed at room temperature and atmospheric pressure for producing nanoparticles in gas phase media (Borra 2006; Meuller et al. 2012; Park et al. 2014; Tabrizi et al. 2009). And nanoparticles generated by this method have been utilized in various applications for their unique optical, electrical and catalytic properties. For example, gold nanoparticles produced by the spark discharge method were employed in organic light emitting diode devices to enhance their quantum efficiency (Sung et al. 2014) and were used as seeds for nanowire growth (Messing et al. 2009). Recent advances have shown that the charged nanoparticles produced by spark discharges can be directed via electrostatic field and assembled into complex three dimensional nanostructures which can be utilized for various applications, for example, in surface enhanced Raman spectroscopy (Jung et al. 2014; Lee et al. 2010) and photovoltaics (Ha et al. 2016; Jang et al. 2016; Kim et al. 2015).

In a spark discharge nanoparticle generation, plasma developed by electrical breakdown of carrier gas between two electrodes vaporizes electrode material. And then, nanoparticles generated from the spark discharge chamber with surrounding ions and charges acquire charges by diffusion charging. However, bipolar charging of nanoparticles has a lower yield of charged particles than unipolar charging (Adachi et al, 1985). Therefore, the yield of nanoparticles generated by the spark

discharge method for electrostatic field controlled patterning was not enough to be used in industrial areas due to their low charging efficiency. Accordingly, in chapter 2, we invented a new type spark control circuit for enhancement of charged nanoparticle generation efficiency. The new type spark control circuit was designed to generate corona discharges between spark discharges such that the charging mechanism could change from bipolar charging to unipolar charging. And then, we confirmed the increased yield of positively charged nanoparticles by using the asymmetric geometry of the electrode which could generate corona discharge.

As nanoparticle utility is increasing, the necessity of scaling up the production rate is also emerging as an important issue. A recent research (Pfeiffer et al 2014) has increased the production rate by using a switchable electronic component for stability control of spark discharge up to a frequency of 20 kHz. However, the geometry of electrodes for mass production of nanoparticles by using spark discharge at high frequencies was not studied before. In chapter 3 of the present study, we investigated the factors which affected the stability of spark discharge at high frequency by comparing different geometries of electrodes: rod-to-rod, rod-to-plate, and wire-to-plate type electrodes. We examined the duration time of spark discharge, which means the time for complete decay of spark discharge at each geometry of the electrodes. Consequently, we confirmed that fast flow rate and strong electric field within the spark zone could enhance the stability of spark discharge.

Lastly, in chapter 4, we invented a wire-to-cylinder type spark discharger for long-term consistent nanoparticle generation by stable operation at high frequency regime. We chose the thickness of the cylinder electrode based on the erosion pattern size of spark discharge and electric field simulation with COMSOL. And we obtained consistent nanoparticle size distribution during 14 hours of spark discharge operation with different frequencies by using the wire-to-cylinder type spark discharger.

Chapter 2.

A Spark Discharger Circuit for Generating Positively Charged Nanoparticles

2.1. Introduction

In a spark discharger, a strong electric field induced by the electrodes causes electrical breakdown of the carrier gas flowing between the electrodes (Meek, 1940). Simultaneously, current flows between the electrodes due to the presence of a conductive plasma that consists of ions and other charged species. The plasma erodes the electrodes locally and vaporizes the material that later condenses into nanoparticles (Tabrizi et al, 2009). These nanoparticles are surrounded by ions and electrons in the plasma, causing the particles to collide into them and acquire charges by diffusion charging (Bau et al., 2010). This phenomenon can be exploited to generate charged nanoparticles, but the bipolar charging of nanoparticles has a lower yield of charged particles than unipolar charging not only because the entire population is divided into more sub-groups (positive, neutral and negative particles, as opposed to just neutral and charged particles) but also because of particle agglomeration due to likely collisions between oppositely charged particles that neutralize both (Adachi et al., 1985). Indeed, injection of unipolar ions from an ionizer has been shown to reduce nanoparticle agglomeration by shifting the charge distribution to one side (Park et al., 2014), although a separate ionizer was installed at a distance from the spark electrodes leading to wasted ions and increased system complexity.

In this chapter, a novel strategy is presented to introduce additional positive ions by utilizing the spark electrodes themselves as the ion source, which eliminates

the need for an additional ionizer. To achieve this, we designed a new spark control circuit to supply positive ions *in situ* via corona discharges as the particles are being generated. Next, we quantified the increased yield of positively charged particles using the new circuit over the conventional circuit in a pin-to-plate spark discharger. Then, the new circuit was implemented with rod-to-plate and wire-in-hole electrode configurations to determine how the electrode geometry affects the generation of charged particles. Finally, the effects of carrier gas flow rate on the charged particle production were studied to investigate the mechanism behind the increased positive particle yield.

2.2. Experimental setup

2.2.1. Spark control circuit

A spark control circuit provides power to the electrodes and controls the spark frequency and energy. The circuits depicted in Figure 2.1 comprise of high voltage power supplies (HVPS, FuG HCP 35-6500), circuit resistors (R_1 , R_2 , 20 M Ω), diodes and circuit capacitors (C , 6 nF). The conventional circuit (Han et al., 2012) is shown in Figure 2.1(a), and has a HVPS (HVPS1, set point $V_1= 6.3$ kV) that is connected in series with the resistor and the pin electrode of the spark discharger. A capacitor is connected in parallel with the resistor and the electrode. The new circuit (Figure 2.1(b)) has an additional power source, which consists of a HVPS (HVPS2, set point V_2), a resistor (R_2) and a diode, connected to the pin electrode in parallel with the conventional circuit. An oscilloscope (Agilent DSO-X 3014A) with a high voltage probe (Tektronix P6015A) was installed to measure the voltage of the electrodes in the spark discharger.

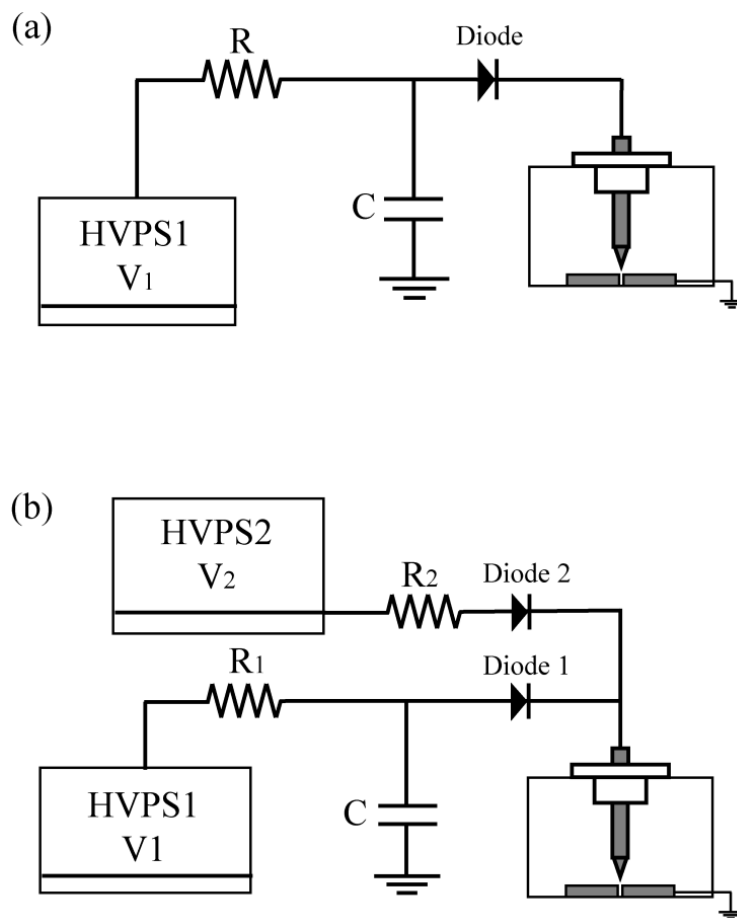


Figure 2.1. (a) Conventional spark control circuit and (b) the modified spark control circuit implemented in this study.

2.2.2. Spark discharger

The spark discharger consists of a cylindrical chamber which has a volume of 26.15 cm³, an inner diameter of 30mm and a height of 37mm. Three different electrode configurations were used in this study: pin-to-plate, rod-to-plate and wire-in-hole. For the pin-to-plate electrode configuration, a 2.35 mm diameter tungsten pin electrode with a sharpened tip was mounted on a holder and aligned to the central axis of the chamber. A stainless steel ground plate with a 2 mm diameter hole was mounted underneath the pin electrode such that the hole is aligned with the pin electrode with a 1.5 mm gap. For the rod-to-plate electrode configuration, everything remained the same except that the pin electrode was not sharpened at its end. For the wire-in-hole electrode configuration (Chae et al., 2015), a different chamber, with 40 mm inner diameter and 30 mm height, was used with a silver wire (0.5 mm diameter, 99.99% purity) and a ground silver plate (99.99% purity) with a hole (2.5 mm diameter). In all cases, a mixture of nitrogen and oxygen (99.999 % purity, N₂:O₂ = 4:1) with flow rates (Q) controlled by mass flow controllers was used as the carrier gas, flowing into the chamber via an inlet and exiting through the hole in the ground plate.

2.2.3. Particle size and charge measurement system

As depicted in Figure 2.2, the chamber outlet is connected to the differential mobility analyzer (DMA, TSI 3085). A stainless steel tube (6.35 mm diameter, 230 mm length) was used to cover the distance between the chamber outlet and the DMA, and a short polyethylene tube was used to connect the stainless tube and the inlet of the DMA to electrically isolate the DMA from the chamber. The DMA was used to quantify particle size distribution from 1-30 nm. The sheath and sampling flow rates of the DMA were 15 and 1.5 lpm, respectively, and the outlet of the DMA was connected to a faraday cup electrometer to obtain current readings which were sent to a computer for data processing. The charged particle size distributions were calculated assuming that particles below 30 nm can only hold charge values of either +1 or -1 (Adachi et al., 1985).

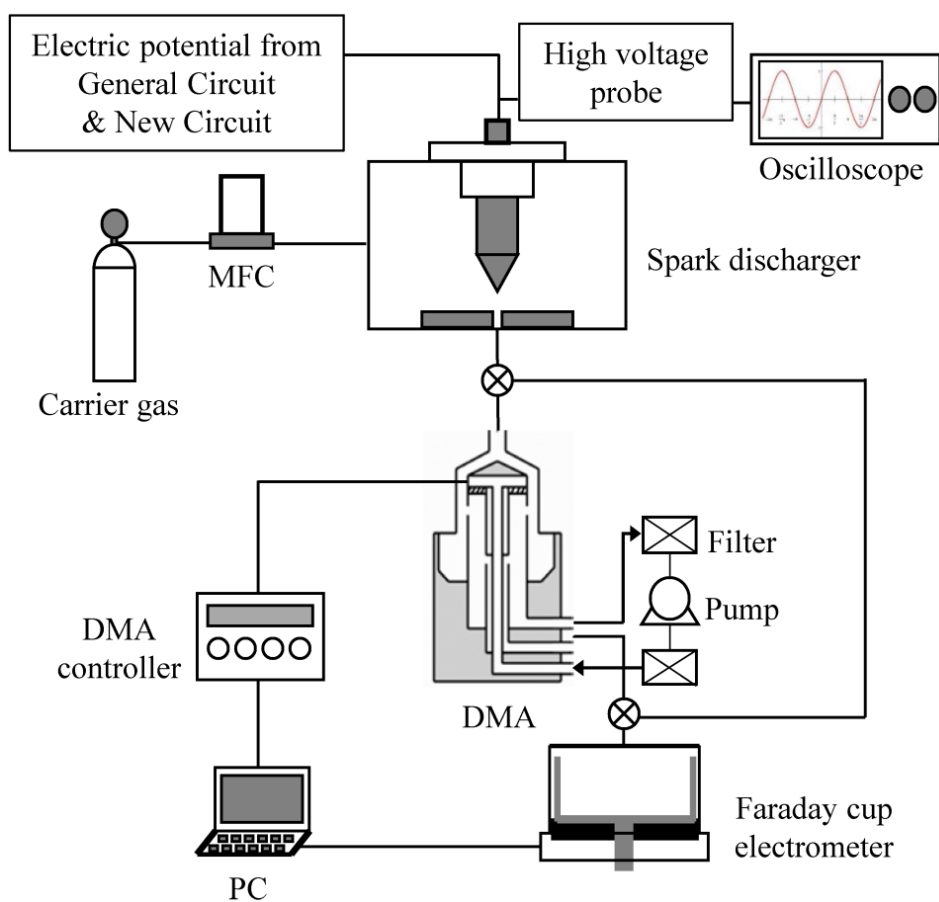


Figure 2.2. Schematic of the experimental setup consisting of spark control circuit, spark discharge chamber (showing pin-to-plate electrodes), and particle number and charge measurement system.

2.3. Results and discussion

2.3.1. Modified spark control circuit

The conventional circuit (Figure 2.1 (a)) is constructed such that the electrodes and the circuit capacitor are always at the same voltage. The circuit capacitor charges over time and discharges electrical energy through the electrodes when the voltage reaches the breakdown voltage of the carrier gas. The capacitor's voltage profile is given by the following equation for the RC circuits:

$$V(t) = V_0(1 - \exp(-t/RC)) \quad (\text{eq.1})$$

Where V_0 is the voltage set by the HVPS, t is the time, R is the resistance of the circuit resistor, and C is the capacitance of the circuit capacitor. The time constant which determines the charging time is $\tau = RC$. The voltage profile generated by the conventional circuit (Figure 2.3(a)) has a saw tooth profile, which means that the electrode voltage is lower than the corona discharge voltage for a significant portion of time in each spark discharge cycle.

In the new circuit (Figure 2.1(b)), the additional power source (HVPS2) does not affect the circuit capacitor as there is a diode (diode 1) that prevents current from HVPS2 flowing into the capacitor. As seen in Figure 2.3(b), after a spark discharge event, the electrode voltage is restored to the set point of HVPS2 (V_2) almost instantaneously. During this time, the capacitor is being recharged by

HVPS1. It is noted that the electrode voltage is restored faster than the capacitor voltage because the additional circuit has a smaller time constant ($C_{\text{electrode}} \ll C_{\text{circuit}}$) than the conventional circuit. Once the voltage across the capacitor exceeds the set voltage value (V_2) of HVPS2, the voltage across the electrodes increases. The diode connected in series with HVPS2 (diode 2) prevents current flowing from HVPS1 to HVPS2. Therefore, the voltage profile of the electrode during this period is similar to that of the conventional circuit. By setting V_2 between the corona discharge voltage and the spark discharge voltage of the pin-to-plate electrodes, corona discharges (which produce positive ions) can be maintained while the capacitor is being charged.

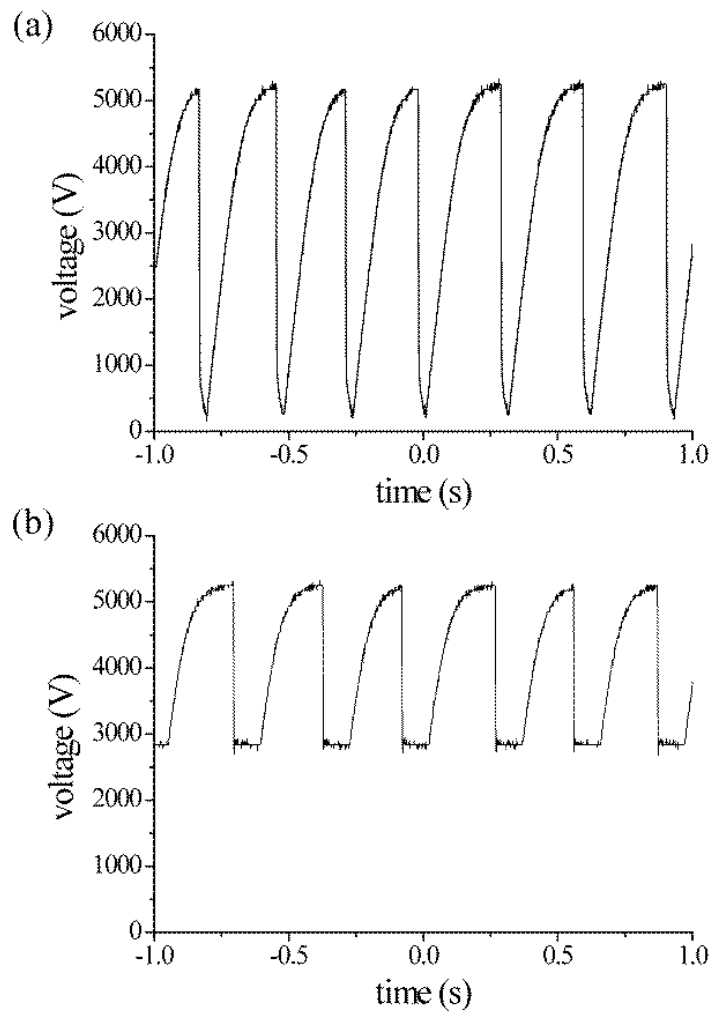


Figure 2.3. (a) A typical saw tooth voltage profile obtained from conventional spark control circuit. (b) Truncated saw tooth voltage profiles at the electrodes where it recovers quickly to the set voltage on the additional high voltage power supply (HVPS2) after a spark discharge event.

2.3.2. Charge measurement from modified spark discharge system

A Faraday cup electrometer was connected to the outlet of the spark discharger to confirm the generation of charged species by the corona discharges. The measured current value increased by approximately 21 pA when V_2 was set to 3400 V (Figure 2.4(a)), which is attributed to both charged particles and other species such as ions. This measured current is proportional to the sum of all charges from both positively and negatively charged species, and therefore, to selectively measure current from charged particles, a DMA was installed between the outlet of the chamber and the Faraday cup electrometer. The effect of varying V_2 on the amount of charged particles generated is shown in Figure 2.4(b). The total current measured from positively charged particles initially increases as V_2 increases, hits the maximum at 3400 V, and decreases thereafter. This can be explained by increased electrostatic losses (Alonso et al., 2006) overcoming the increased yield from positively charging at higher voltages. In the case of negative particles, the magnitude of measured current decreases as V_2 increases as expected. At 3400 V, the total current measured from positively charged particles and negatively charged particles increased by 4 pA and 2 pA, respectively. These changes correspond to an 88% increase for positively charged particles and 46% reduction for negatively charged particles.

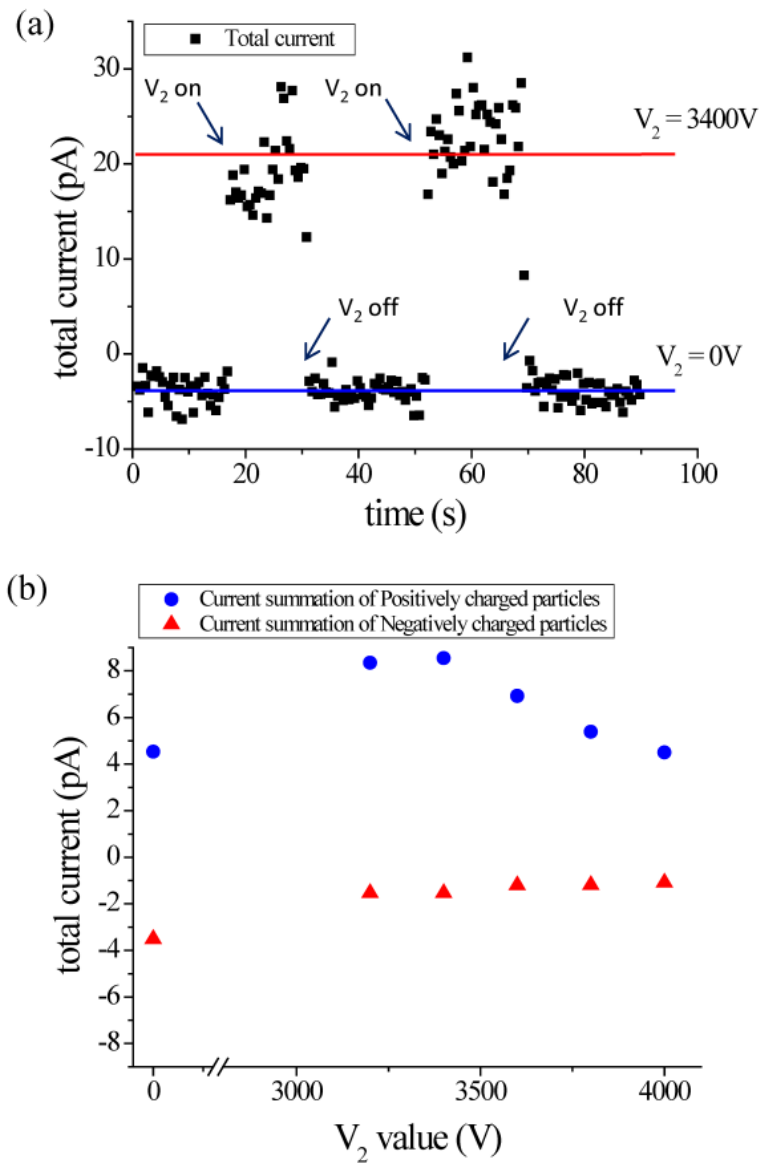


Figure 2.4. (a) Total current measured by the Faraday cup electrometer directly from the outlet of spark discharger with $V_2 = 3400$ V. (b) The current from charged particles only measured by Faraday cup electrometer after DMA filtering at various V_2 voltages.

It should be noted that this current increase from the charged particles (6 pA) is smaller than the total current increase measured by the Faraday cup electrometer connected directly to the outlet of the spark discharger (21 pA). Since the faraday cup picks up all charged species, the discrepancy between the faraday cup measurements and the DMA measurements can be attributed to the existence of excess positive ions, confirming that the fast electrode potential recovery enabled by HVPS2 does indeed lead to increased positive ion generation, which in turn results in more positively charged particles.

2.3.3. Size distribution of charged particles

Then, we looked more closely at the effect of V_2 on the size distribution of the generated particles. Figure 2.5 shows the comparison of charged particle size distributions with V_2 values of 3400 V and 0 V generated using the spark discharger with pin-to-plate electrodes. When the V_2 value was set to 0 V, the new circuit is essentially the same as the conventional circuit, therefore both distributions for positively and negatively charged particles are similar. When V_2 was set to 3400V, not only did the total amount of positively charged particles increase, but the mode value of their size (we will refer to this value as the representative ‘particle size’) shifted from 10 nm to 7 nm. This shift is expected as increased amount of positive ions available will prevent agglomeration of nanoparticles by charging them to the same polarity. Figure 2.6(a) and 2.6(b) show particle size distributions for each polarity using various V_2 values. For positively charged particles, the generated amount increases until 3400 V. Above 3400 V, the particle size and the amount decreased as V_2 further increased, which can be attributed to increased electrostatic losses as discussed above. At 4000 V, the yield returned to similar levels as 0 V, albeit with a different size distribution, hence it is no longer advantageous to increase V_2 further. These trends are consistent with previously published studies (Park et al., 2014). On the other hand, the amount and size of negatively charged particles decreased as V_2 increased, as both increased supply of positive ions and electrostatic losses lower their yield.

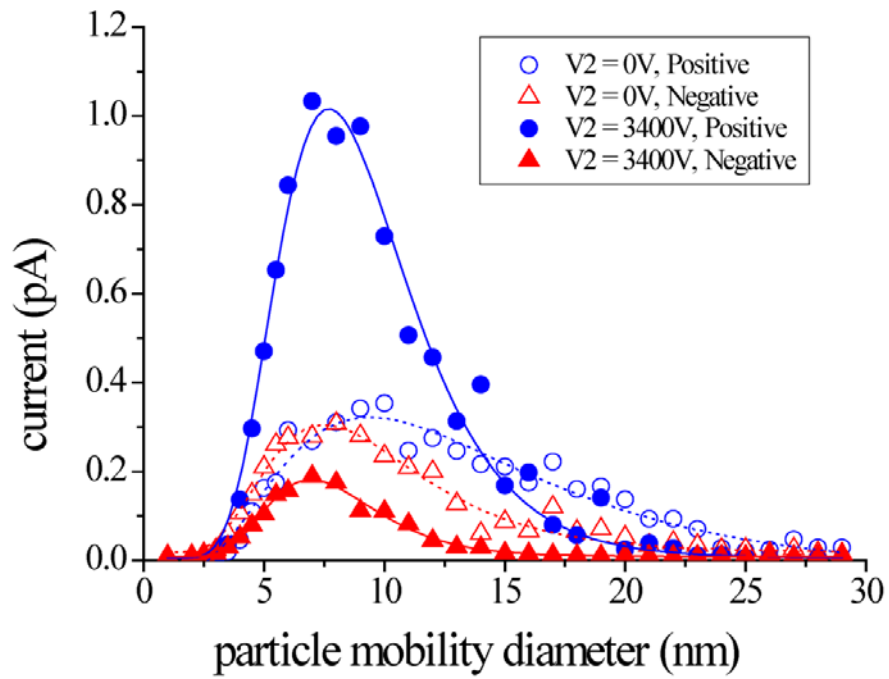


Figure 2.5. Charged particle size distributions obtained by using the modified spark control circuit at $V_2 = 3400$ V.

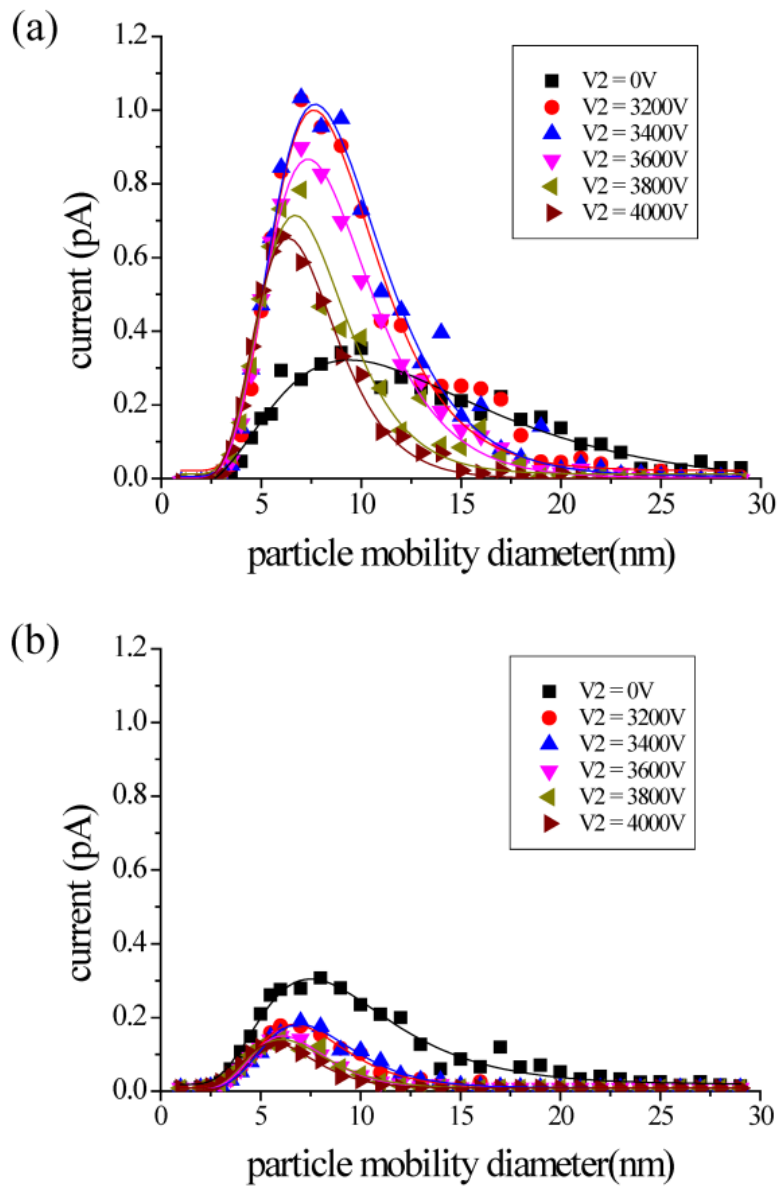


Figure 2.6. (a) Positively charged particle size distributions, and (b) negatively charged particle size distributions obtained by using the modified spark control circuit with various V2 values.

2.3.4. Effects of electrode geometry

Figure 2.7 shows how various electrode configurations perform with the new circuit to produce positively charged particles. The performance of the rod-to-plate electrodes and wire-in-hole (Chae et al., 2015) electrodes were compared to that of pin-to-plate type electrodes. In the case of rod-to-plate electrodes, there was no increase in the quantity of positively charged particles when HPVS2 was turned on (Figure 2.7(a)) as the uniform electrostatic field induced by the rod-to-plate electrodes did not generate corona discharges, but rather generated arc discharges that do not contribute additional positive ions (Hinds, 1999). In fact, the charged particle yield was lower due to larger electrostatic losses caused by large V_2 . In the case of wire-in-hole electrodes, corona discharges were induced, and hence the yield of positively charged particles increased (Figure 2.7(b)) following the same mechanism as the pin-to-plate configuration. The wire-in-hole configuration is able to generate particles for a prolonged time (Chae et al., 2015), and hence it is expected that the new circuit used in conjunction with the wire-in-hole electrode configuration will generate positively charged particles with enhanced yield.

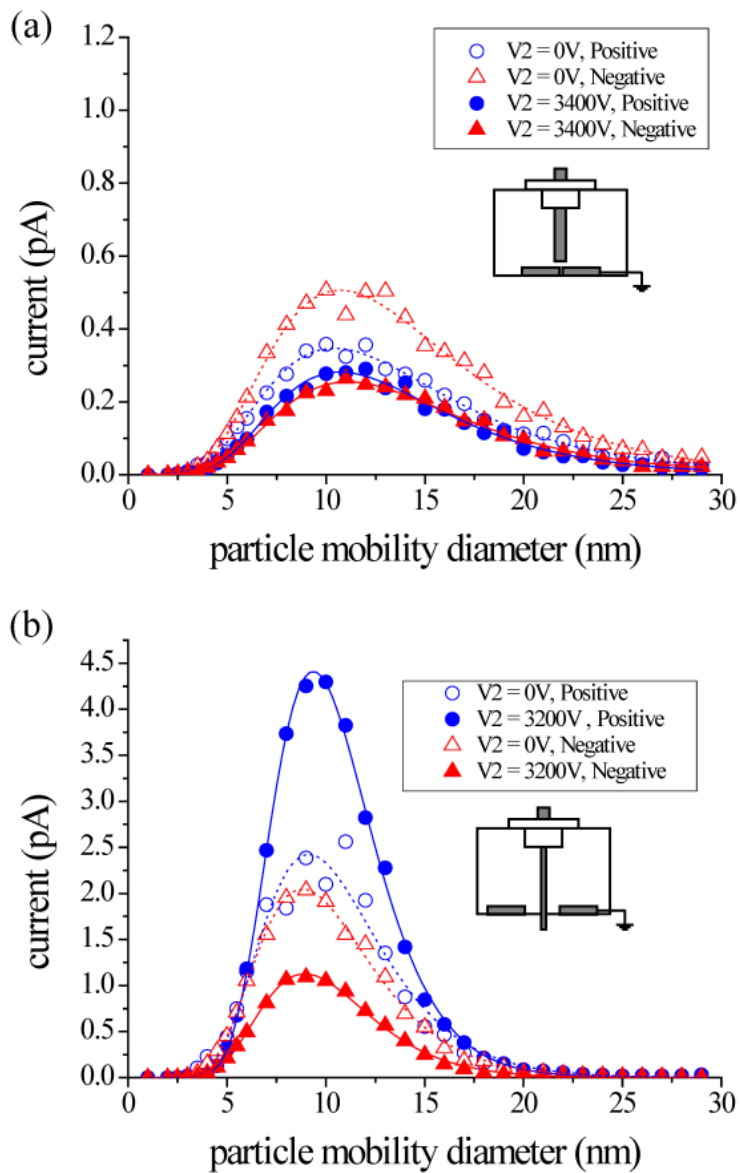


Figure 2.7. Particle size distributions obtained by using the new spark control circuit with various electrode configurations; (a) rod-to-plate and (b) wire-in-hole configuration.

2.3.5. Effects of flow rate

Finally, the effect of carrier gas flow rate on the charged particle generation using pin-to-plate electrodes was studied (Figure 2.8). The positively charged particle production enhancement diminishes from 88 % to 27 %, then to 18 % when the carrier gas flow increases from 1.5 lpm, to 4 lpm and to 6 lpm. A higher carrier gas flow rate is expected to reduce the particle and ion concentration and their residence time in the corona discharge region, lowering the probability of diffusion charging of the particles. Hence, the fact that increased yield is not present at high carrier gas flow rate supports that the corona-generated ions were responsible for the increased yield of positively charged particles shown in this study.

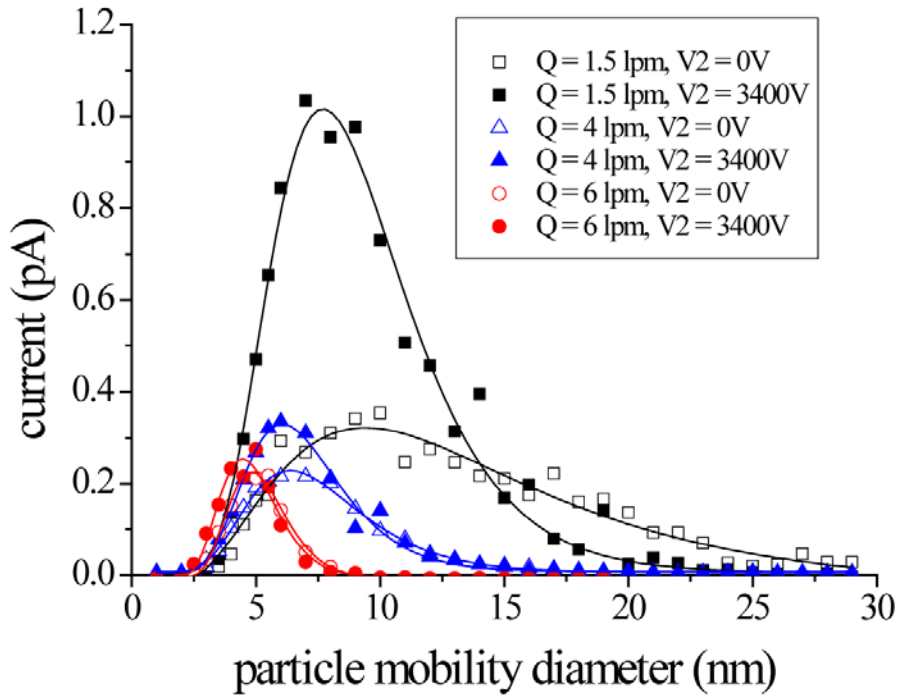


Figure 2.8. The effect of carrier gas flow rate on positively charged particle size distributions with pin-to-plate configuration. The positive particle yield enhancement diminishes at high flow rates.

2.4. Conclusion

We have designed and implemented a new spark control circuit which increases the yield of positively charged particles in comparison to the conventional circuit in a spark discharger. The new circuit was designed to rapidly restore the electrical potential of the anode to maintain corona discharges while the circuit capacitor is being charged. Using a Faraday cup electrometer to directly capture of all charged species at the outlet of the spark discharge chamber has shown approximately 21 pA increase in the total current when V_2 was set at 3400 V. The contributions from positively and negatively charged particles were measured separately by implementing a DMA, and they were approximately 4 pA and 2 pA, which correspond to 88% increase and 46% decrease in yield, respectively. The size distributions of charged particles shifted toward smaller sizes, which indicates that the increased supply of positive ions charges nanoparticles, leading to less agglomeration. The electrode configuration was found to play an important role in increasing charged particle yield using the new circuit. The rod-to-plate configuration does not induce corona discharges and therefore no increase in positive particle yield was observed. The wire-in-hole configuration does induce corona discharges, hence was able to take advantage of the new circuit to increase the production of positive particles. Last, we showed that at high carrier gas flow rate, the increase in positive particle yield is suppressed, which confirms that the diffusion charging of particles as they are produced is critical. In conclusion, the

new spark control circuit developed in this work is an effective and facile approach to increase the positively charged particle yield from a spark discharger without installing additional components such as ionizers, and in conjunction with the wire-in-hole electrode configuration, has a potential to scale up charged particle production for cutting edge applications such as three-dimensional electrostatic assembly of nanoparticles.

Chapter 3.

A Study of Spark Dischargers for Stability Control in High Frequency Region

3.1. Introduction

To integrate spark discharge generated nanoparticles into industrial applications, the ability to scale up the manufacturing process in a uniform and stable manner is essential. Multi sets of spark electrodes have been conducted to scale up nanoparticle production rate (Ha et al. 2014; Efimov et al 2013; Efimov et al 2016). However, optimization of single set of electrodes has not widely been researched yet. There are many ways to increase the production rate of a single set of electrodes, one of which is to increase the spark frequency. Each spark discharge can be thought of as a unit event that generates a certain amount of nanoparticles, and the production rate is expected to scale linearly with the spark frequency. In reality, this is not the case as at high frequency regime above 1 kHz, premature spark discharges occur intermittently, resulting in a production rate that is lower than expected (Pfeiffer et al. 2014). Of note, a recent review article has demonstrated spark stability up to 20 kHz by adding fast switching electronic components to the conventional circuit to prevent premature spark discharges and to regulate the spark duration.

In this study, we sought to stabilize the spark discharge process at high frequencies by first determining the factors which affect the spark stability. We hypothesized that the residual spark plasma is the cause of premature spark discharges, and hence developed a wire-to-plate electrode configuration which has increased local carrier gas flow velocity and electric field intensity around the spark

zone, both of which are expected to contribute to fast removal of spark plasma generated by the preceding spark event. The maximum stable spark frequency and spark duration of wire-to-plate electrodes were compared against those of rod-to-rod and wire-to-rod electrodes and the effect of the electric field intensity and gas velocity were confirmed separately. Then, the nanoparticle production rates were quantified for high frequency operations to confirm that the production rates scale up as expected. Lastly, changes in their size distributions depending on the operating frequency were noted and their implications were discussed.

3.2. Experimental setup

3.2.1. Three electrode geometries of spark dischargers

The spark discharger was constructed using a custom cylindrical chamber (122 cm³ volume, 50 mm inner diameter, 62 mm height). Three different electrode configurations were used in this study: rod-to-rod (Figure 3.1(a)), wire-to-rod (Figure 3.1(b)) and wire-to-plate (Figure 3.1(c)). Copper rods (diameter, $d = 7$ mm) and wires ($d = 1$ mm) were used as electrodes for rod-to-rod and wire-to-rod configurations, and were installed horizontally and coaxially within the spark discharge chamber. For wire-to-plate type electrode configuration, a copper wire ($d = 1$ mm) electrode was installed vertically on a holder and aligned to the central axis of the chamber. Then, a copper ground plate (which also serves as the cathode in this configuration) with a 0.5 mm diameter hole was mounted underneath the wire such that the hole is coaxially aligned with the wire electrode.

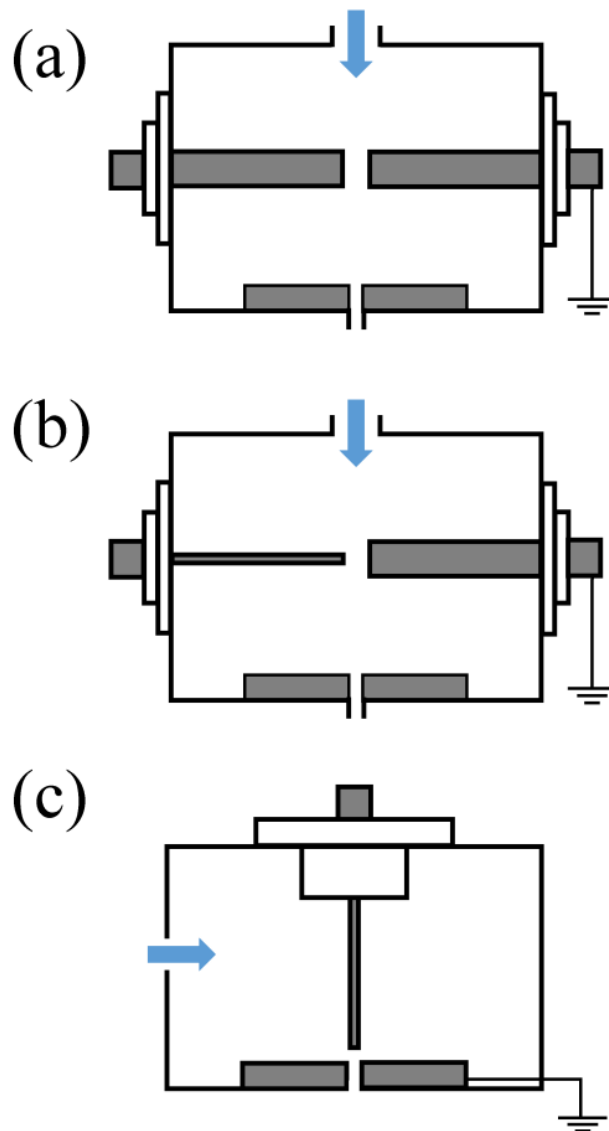


Figure 3.1. Three different electrode configurations (a) rod-to-rod, (b) rod-to-plate and (c) wire-to-plate. Blue arrows indicate carrier gas inflow

3.2.2. Spark discharge and measurement system

The experimental setup shown in Figure 3.2 was used to generate nanoparticles and measure the size distribution of the produced nanoparticles as well as to measure the voltage and current at the electrodes during the process.

The ‘conventional’ circuit was used to control the spark discharge (Chae et al. 2015; Han et al. 2012), comprising of a high voltage power source (HVPS, FuG HCP 350-12500), a resistor (200 or 400 k Ω) and a capacitor (1, 2 or 3 nF). The spark frequency was controlled by varying the voltage input from the HVPS and the resistance of the circuit, while other parameters (discharge voltage, mass flow rate of carrier gas and capacitance of the circuit) remained unchanged. An oscilloscope (Agilent DSO-X 3014 A) equipped with a high voltage probe (Tektronix P6015A) and a current probe (Agilent 1147A) was connected to the anode for voltage and current measurements.

For all experiments, nitrogen (99.999 % purity) was used as the carrier gas, and its flow rate was controlled using a mass flow controller. The gas flow was directed such that it enters through the chamber inlet and exits through the hole ($d = 0.5$ mm) in the copper ground plate (In the rod-to-rod and wire-to-rod cases, the plate was still mounted to the chamber to keep the flow conditions the same as the wire-to-plate case.). The anode (wire electrode in the wire-to-rod configuration) was connected to the spark control circuit, and the cathode was connected to the ground. The gap between the electrodes was adjusted to set the discharge voltage at 2.2 kV.

The particle size distribution measurement system consists of a differential mobility analyzer (DMA, TSI 3085), a DMA controller (TSI 3776), and a condensation particle counter (CPC TSI 3776). The DMA and CPC were used in conjunction to quantify the nanoparticles generated from the spark discharger in the range of 4-150 nm, and to obtain the particle size distribution.

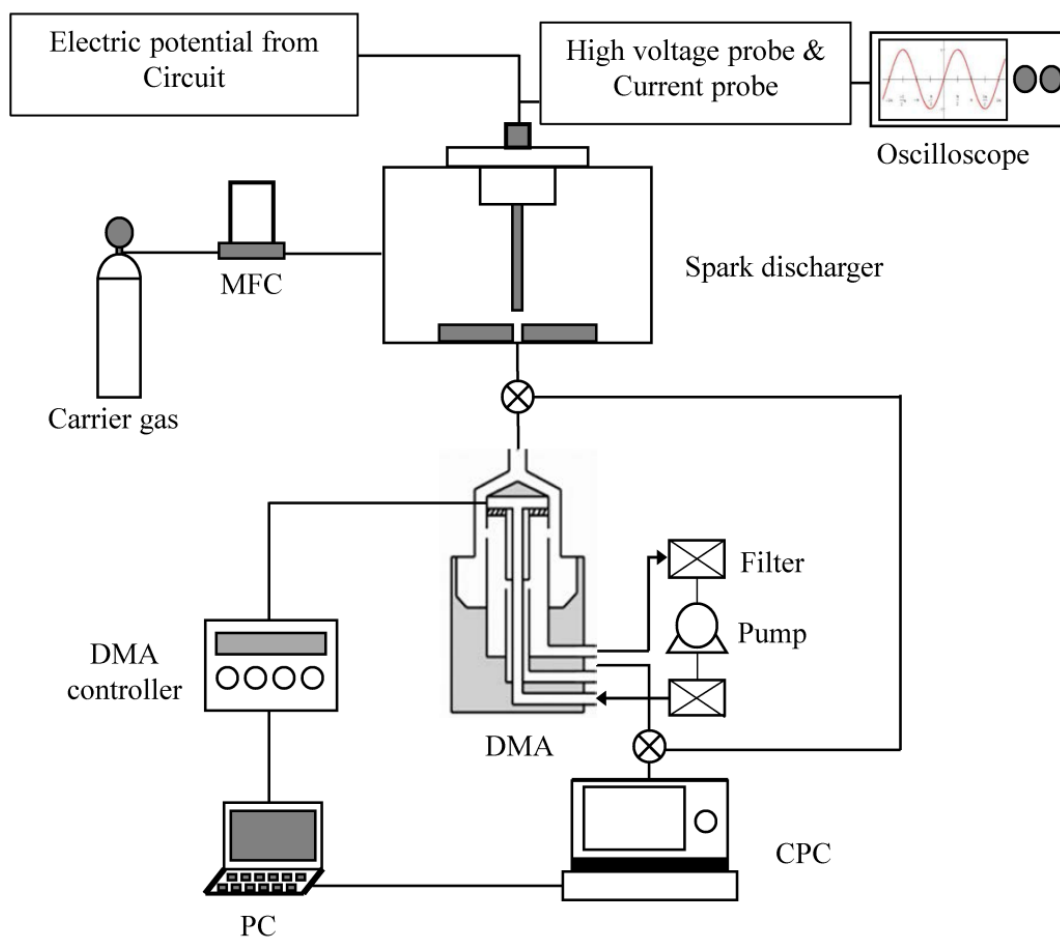


Figure 3.2. Schematics of experimental setup showing wire-to-plate electrode configuration as an example.

3.3. Results and discussion

3.3.1. Unstable state of spark discharge with Rod-to-rod electrodes

For a spark discharge to occur, the voltage across the electrodes must exceed the breakdown voltage of the medium between them. Once the voltage exceeds the threshold value, dielectric breakdown of the medium occurs, and spark plasma is generated, which completes the circuit and a current flows through the gap between the electrodes. Once the capacitor is discharged completely, the cycle starts again.

To determine the stability of the spark events, we monitored the voltage profiles across the spark electrodes using an oscilloscope and a high voltage probe. Figure 3.3(a) depicts an exemplary voltage profile of a stable spark discharge process with rod-to-rod electrodes where the spark discharge events occur at the desired voltage (~2.2 kV) consistently at a frequency of 1.1 kHz. When the spark frequency is increased to approximately 3.7 kHz, premature spark discharge events occur and spark discharge voltages as low as 600 V were observed (Figure 3.3(b)). The premature spark discharge occurs due to reduced breakdown voltage of the medium caused by residual space charge coming from the spark plasma that has not been completely removed (Pfeiffer et al. 2014). Therefore, to prevent premature spark discharges (or at least increase the onset frequency), it is necessary to restore the medium to its ‘normal’ state as quickly as possible before the next spark discharge

event. The time needed for complete removal of the plasma may depend on a number of factors, such as the electrode geometry and configuration, carrier gas velocity and the spark discharge voltage.

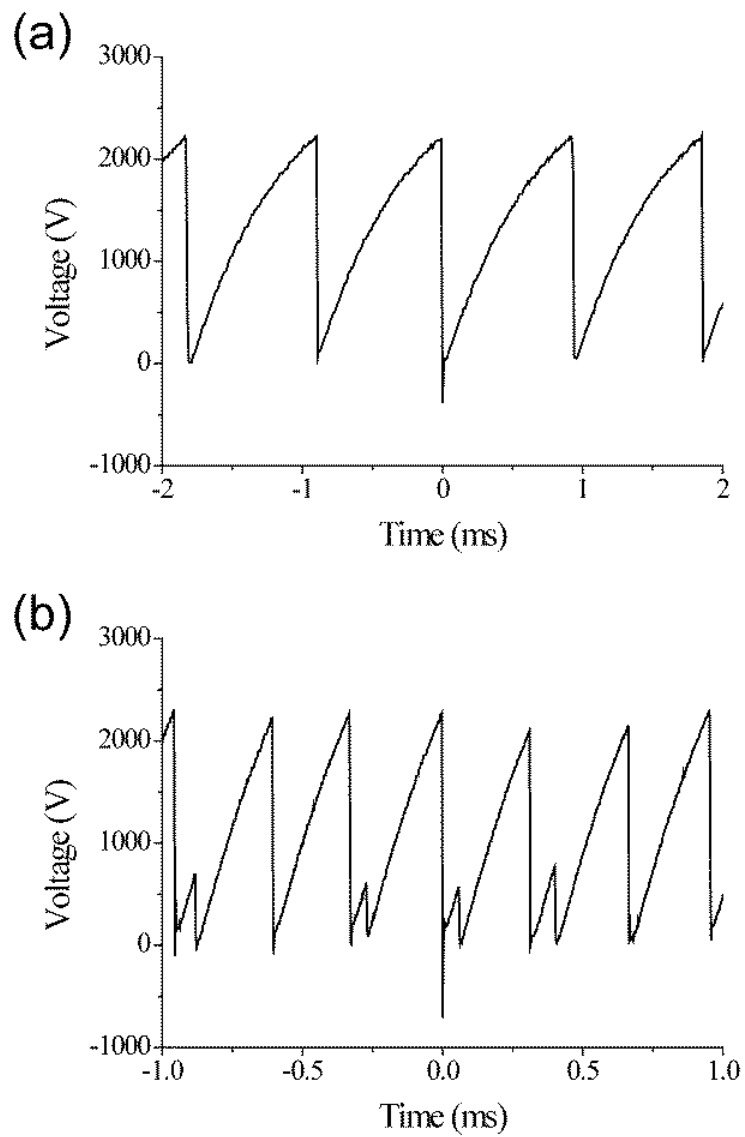


Figure 3.3. Voltage profiles from rod-to-rod electrode type spark discharger. (a) Frequency of 1.1 kHz. (b) Frequency of 3.7 kHz; unstable state with discharge voltages below the desired breakdown voltage (2.2 kV)

3.3.2. Spark duration time analysis

Three electrode configurations were examined to identify the factors that affect the spark stability: rod-to-rod, wire-to-rod and wire-to-plate. Using 6.7 lpm carrier gas flow, the maximum stable spark frequency was 1.1 kHz for rod-to-rod configuration, 2 kHz for wire-to-rod configuration, and 17.9 kHz for wire-to-plate configuration. This can be understood in terms of how fast the spark plasma is removed, and the medium returns to the 'normal' state. Indeed, at spark frequency of 1 kHz and carrier gas flow rate of 6.7 lpm, the voltage and current profiles of the three configurations show that the spark duration (defined as time for voltage/current oscillation to completely decay) is 5.45, 5.05, and 4.78 μ s for rod-to-rod, wire-to-rod and wire-to-plate configurations respectively (Figure 3.4), where shorter duration is indicative of faster plasma removal. The differences in spark duration can be explained by electrical repulsion from the high-intensity electric field and physical removal by the local carrier gas flow. The rod-to-rod and wire-to-rod configurations have similar local carrier gas velocity due to their geometric similarity, but the wire electrode in wire-to-plate configuration produces larger electric field intensity because of its thinner diameter, and hence the plasma is displaced faster by electrical repulsion. The wire-to-plate spark discharge generator was able to produce regular sparks at the highest frequency, which can be attributed to the fast local flow velocity near the spark region, in addition to the high electric field intensity arising from the wire electrode (Han et al. 2012).

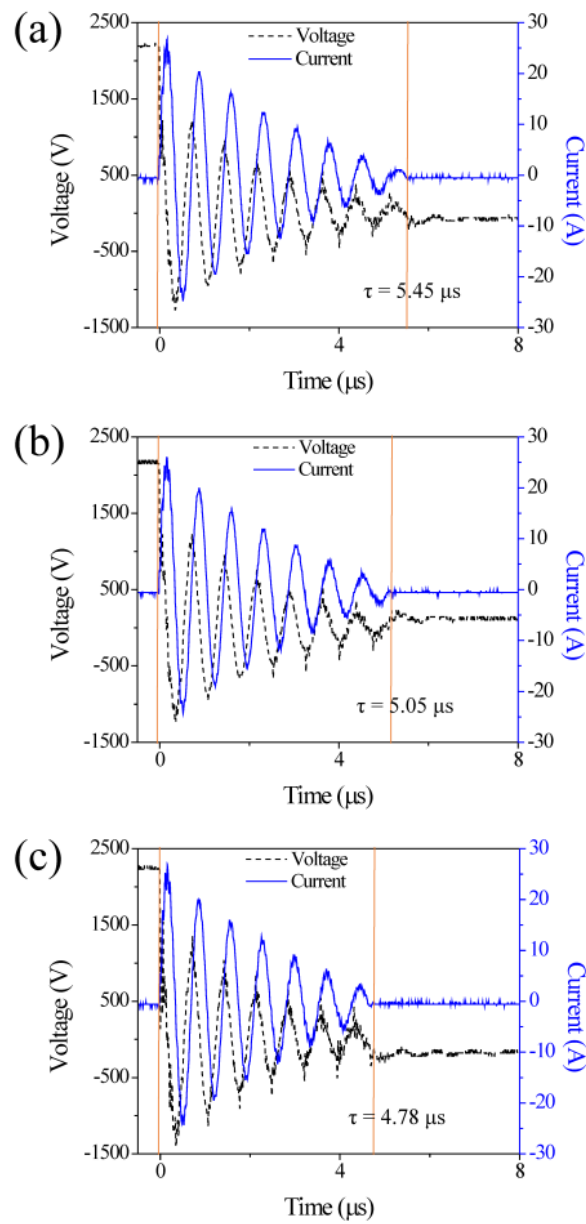


Figure 3.4. Current and voltage profiles during spark discharge events at 1 kHz spark frequency. (a) rod-to-rod, (b) wire-to-rod, and (c) wire-to-plate electrode configuration.

3.3.3. Electrical effects on the spark duration time

To validate the role of electric field intensity in spark discharge stabilization, we have measured the spark duration at different frequencies at a fixed carrier gas flow rate of 6.7 lpm (Figure 3.5). The average spark duration time decreased from 4.78 to 2.05 μs as the spark frequency increased from 1 kHz to 17.9 kHz. As faster restoration of the electrode potential leads to stronger electric field intensity, this result indicates that higher intensity electric fields help remove plasma faster, and thereby help stabilize the spark discharge process at high frequencies.

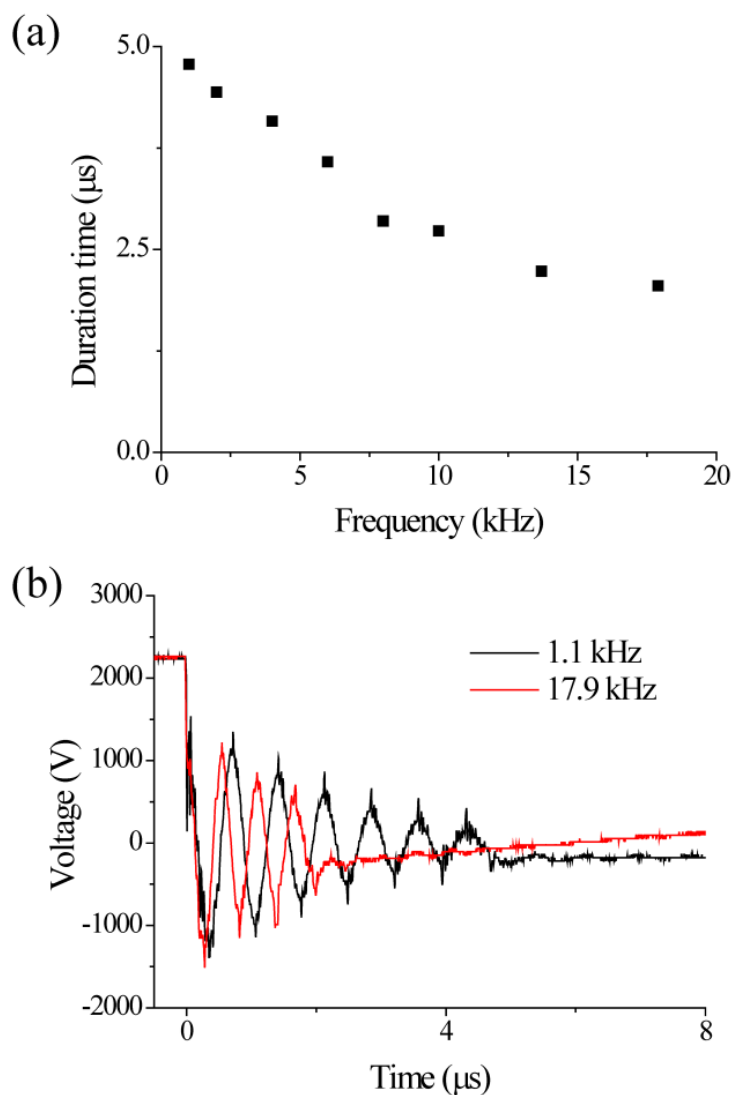


Figure 3.5. (a) Spark duration time of wire-to-plate electrode type spark discharger as spark frequency increases (Capacitance 1nF, breakdown voltage 2.2 kV, N₂ flow rate 6.7 lpm. (b) Voltage profiles during spark discharge events at 1.1 kHz and 17.9 kHz.

3.3.4. Flow rate effects on the stability of spark discharge

To confirm that the faster carrier gas flow helps stabilize spark events at higher frequencies, the voltage profiles for wire-to-plate electrodes set up for 14 kHz spark frequency using flow rates of 4.1 and 6.7 lpm were compared. At 4.1 lpm, premature spark discharges below the desired voltage of 2.2 kV occurred intermittently because the slow carrier gas flow was unable to eliminate the plasma between the electrodes (Figure 3.6(a)). At 6.7 lpm, the spark events occurred regularly, discharging at the desired voltage of 2.2 kV (Figure 3.6(b)). These results show that the faster carrier gas flow rate is indeed beneficial for high frequency operation of spark dischargers.

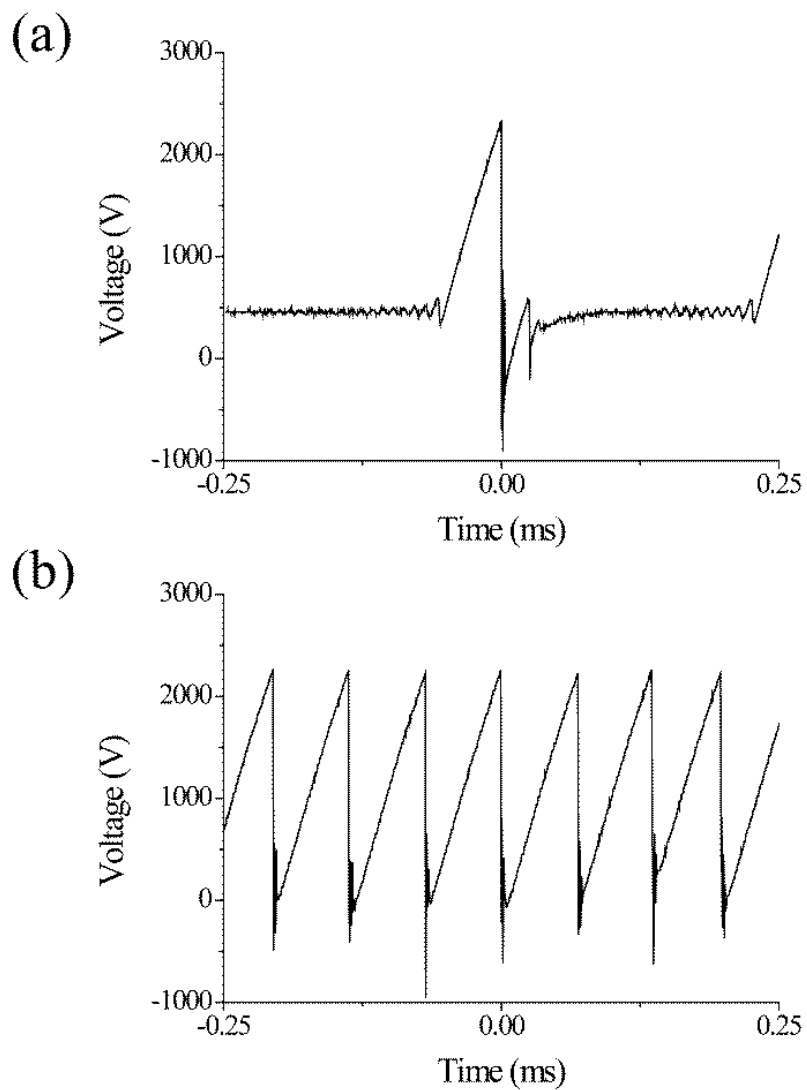


Figure 3.6. Voltage profiles from wire-to-plate electrode type spark discharger with frequency of 14 kHz with carrier gas (N₂) flow rates of (a) 4.1 lpm and (b) 6.7 lpm.

3.3.5. Mass production rate analysis

In addition to the stability of the spark events, we quantified the production rates of nanoparticles at different carrier gas flow rates. We chose the mass production rate to represent the production rate of nanoparticles, which can be approximated by the electrode ablation rate. The electrode ablation rate was measured by weighing the electrodes before and after spark discharge operations. The mass production rate should increase linearly with the spark frequency, as long as premature spark discharges do not occur. Indeed, it was seen that with 4.1 lpm carrier gas flow, the mass production rate linearly increased with the frequency, up until ~14 kHz, after which premature spark discharges developed and the mass production rate dropped off sharply. On the other hand, with 6.7 lpm flow, the mass production rate continued to increase linearly all the way up to 17.9 kHz (Figure 3.7(a)). The mass production rates measured within stable spark frequency range were consistent irrespective of the carrier gas flow rate, which means that electrode ablation does not significantly depend on the carrier gas flow. The mass production rate also showed linear dependence on the circuit capacitance as expected (Figure 3.7(b)), and this shows that increasing the spark energy does not interfere with the spark stability. The electrode ablation efficiency was calculated to be 0.234×10^{-7} gJ⁻¹ based on the total energy stored in the capacitor before discharge.

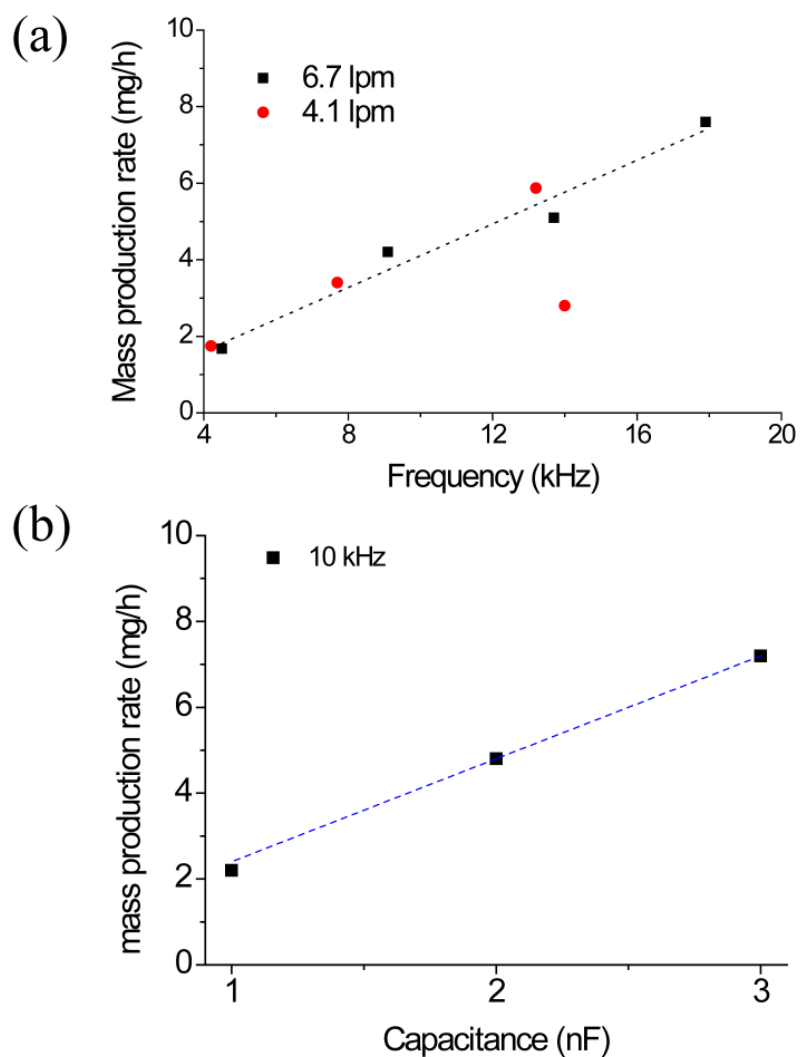


Figure. 3.7. Mass production rate of nanoparticles (Cu) scale linearly with (a) spark frequency (Capacitance 2 nF), up to the maximum stable spark frequency, and (b) external capacitance, at spark frequency of 10 kHz and flow rate of 6.7 lpm.

3.3.6. High frequency spark discharges with Wire-to-Plate electrodes

Lastly, the particle size distributions were measured for spark frequencies of 4.5, 9.1 and 17.9 kHz to observe the effect of changing the spark frequency, while the carrier gas flow rate was kept at 6.7 lpm. Figure 3.8 (a), (b) and (c) show that the spark events are indeed stable for the tested frequencies of 4.5, 9.1 and 17.9 kHz, respectively. As seen in Figure 3.9, the geometric mean diameters were 11.0, 21.5 and 36.7 nm and the standard deviations were 1.40, 1.48 and 1.50, respectively. While the increase in spark frequency in a stable spark event leads to a linear increase in the mass production rate, the total number concentration and the mean particle diameter also increases with little changes to the standard deviation. It was expected that the flow conditions around the electrodes remain the same while increased spark frequency vaporize more material in a given time, leading to higher concentration of primary particles that later agglomerate and thus larger mean particle agglomerate diameters. (Tabrizi et al. 2009). This suggests that the particle size distributions of aerosol can be tuned according to the intended application either by increasing the gas flow rate (above the minimum gas flow rate that ensures stable high frequency operation) or by adding a clean gas flow (dilution) downstream of the spark generator.

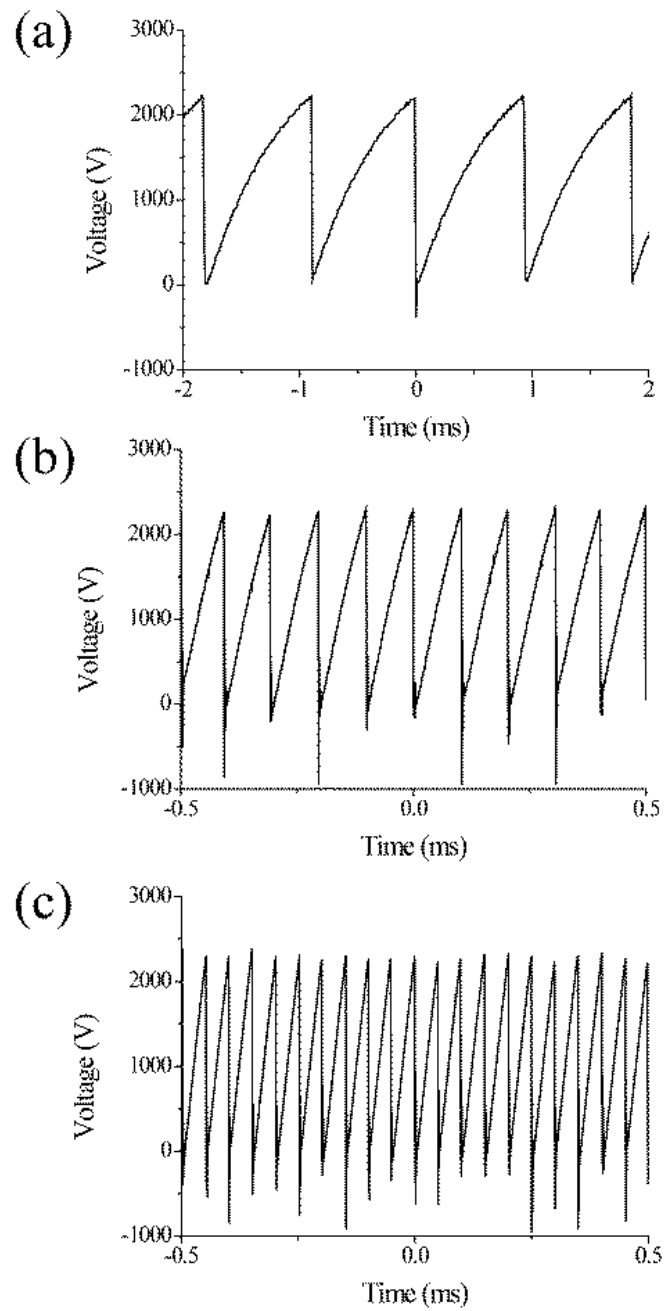


Figure 3.8. Voltage profiles from wire-to-plate electrode type spark discharger at different frequency: (a) 4.5 kHz, (b) 9.1 kHz and (c) 17.9 kHz.

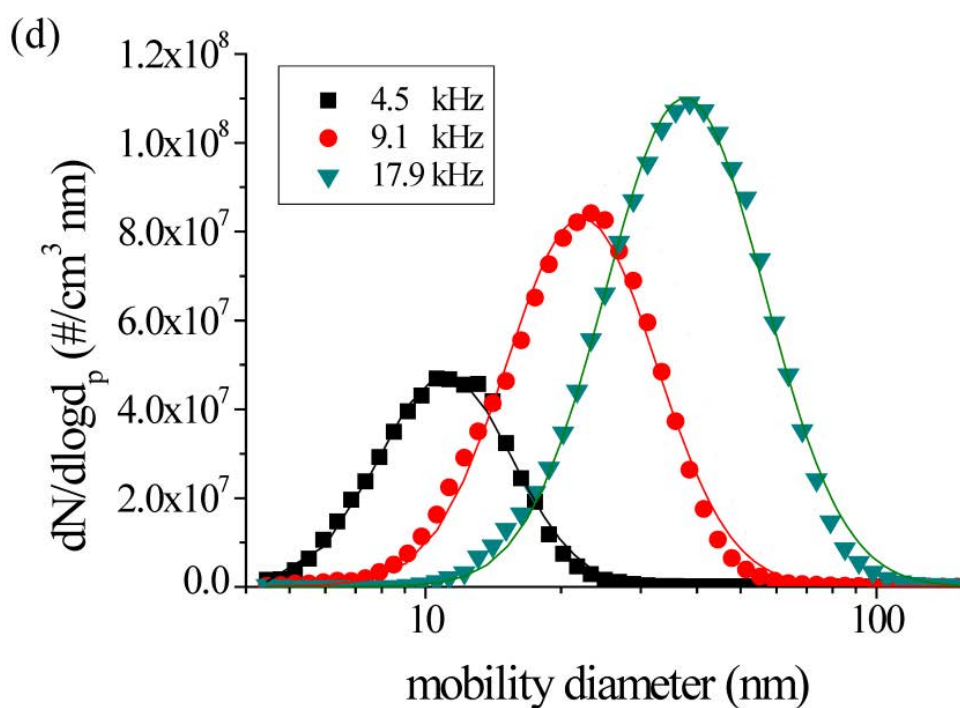
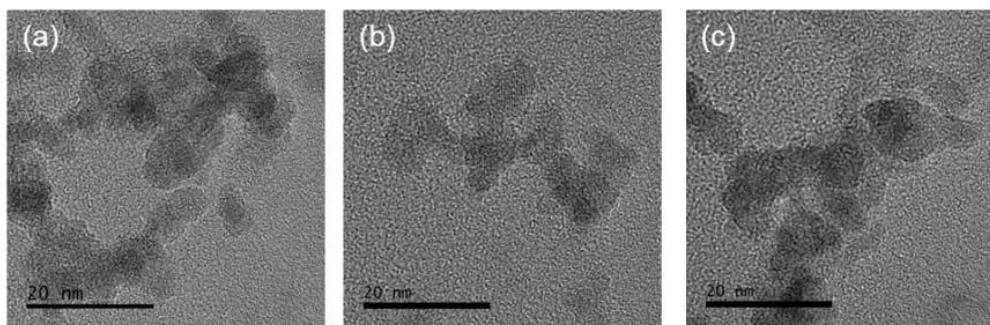


Figure 3.9. TEM images of agglomerated copper nanoparticles generated at (a) 4.5 kHz, (b) 9.1 kHz, and (c) 17.9 kHz. (d) Size distribution of generated nanoparticles at each frequency showing increasing geometric mean diameter and total number concentration as the frequency increases. The energy per spark and the gas (N₂) flow rate are 4.84 mJ and 6.7 lpm in all the cases.

3.4. Conclusion

We have developed a high frequency spark discharge generator using wire-to-plate electrode configuration that enables fast removal of spark plasma and have compared its performance to rod-to-rod and wire-to-rod electrode configurations to identify process parameters that determine the maximum stable spark frequency. By observing the current and voltage profiles of the spark discharge events, rapid plasma removal characterized by short spark duration was identified as an important feature of stable spark discharges at high frequencies for our wire-to-plate electrode spark discharger. High-intensity electric fields and fast carrier gas flows within the spark zone were both found to contribute to faster plasma removal, and therefore to stable high frequency operation. Among the three electrode configurations compared, wire-to-plate electrodes were best suited to implement both means, achieving spark stability up to 17.9 kHz. Using the wire-to-plate electrodes, it was shown that the mass production rate of nanoparticles indeed scale linearly with the spark frequency as long as no premature spark discharges occur. Increasing the spark frequency leads to particle agglomerates of increasing mean diameter, and hence appropriate measures should be taken when designing large industrial-scale spark discharge generators for production of nanoparticles with a specific size distribution.

Chapter 4.

Wire-to-Cylinder Type Spark Discharger for Long Time Consistent Nanoparticle Generation

4.1. Introduction

The rod-to-rod type electrode has been widely researched in the spark discharge nanoparticle generation because of its geometric convenience and durability with generating nanoparticles (Horvath and Gangl 2003; Evans et al. 2003; Tabrizi et al. 2009). However, the nanoparticle generated by the rod-to-rod type spark discharger has a tendency of agglomeration at high concentration of nanoparticle generation. To overcome this problem, high flow rate carrier gas has been used for generating nanoparticles with smaller size distribution (Pfeiffer et al 2014). In an electrode geometric approach, a pin-to-plate electrode type spark discharger which could achieve fast carrier gas velocity in vicinity of the spark discharge was introduced (Han et al 2012). And this geometry could generate less agglomerated nanoparticles than the rod-to-rod electrode type spark discharger in the same carrier gas flow condition. Nevertheless, the pin-to-plate type electrode was not proper to generate nanoparticles in industrial areas because the hole size of the plate electrode became larger due to the erosion from the spark discharge operating in a long time. And this could hinder the consistent nanoparticle generation with maintaining the similar particle size distribution. To enhance the durability of nanoparticle generation by spark discharge, a wire-in-hole electrode type spark discharger was proposed (Chae et al 2015). However, this research also had a limitation which could not maintain the hole size consistently.

In this study, we invented a wire-to-cylinder type electrode which could generate less agglomerated nanoparticles than rod-to-rod electrode and maintain the size distribution of nanoparticle in long-time spark discharge operation. We conducted the electric field simulation between the wire and the cylinder electrode for determining proper thickness of cylinder wall. Finally, we maintained the spark discharge operation for 14 hours and obtained the consistent nanoparticle size distribution during the spark operation time.

4.2. Experimental setup

4.2.1. wire-to-cylinder type electrode spark discharge nanoparticle generation system

With the same cylindrical chamber (122 cm³ volume, 50 mm inner diameter, 62 mm height) as used in chapter 3, the wire-to-cylinder electrode configuration was employed in this chapter (Figure 4.1). Copper rod wire (d = 1 mm) and cylinder (inner diameter = 1.6 mm, outer diameter = 2 mm) were used as electrodes, and were installed horizontally and coaxially within the spark discharge chamber. A copper cylinder electrode which was machined on the cylinder holder was mounted underneath the wire such that the cylinder is coaxially aligned with the wire electrode. A general external circuit was used for the spark discharge particle generation system. The electrical energy of a spark discharge in the spark discharger was provided from the external circuit which could alter the frequency and the emitting energy of the spark. The circuit depicted in Figure 4.1 was composed of the high voltage power supplies (HVPS, FuG HCP 35-6500), external resistors (660 kohm) and an external capacitor (C_{ext}, 1nF). In the general external circuit, a HVPS was connected in series through the resistor to the electrode of the spark discharger. The external capacitor was connected in parallel to the HVPS. The charging rate of the capacitor could be controlled by changing the resistance of the external resistor. The electrical energy charged in the external capacitor was sent to the electrode of

the spark discharger when the voltage of the external capacitor reached the break down voltage of the spark discharger. Nitrogen (99.999 % purity) was used as the carrier gas which was regulated by the mass flow rate controller.

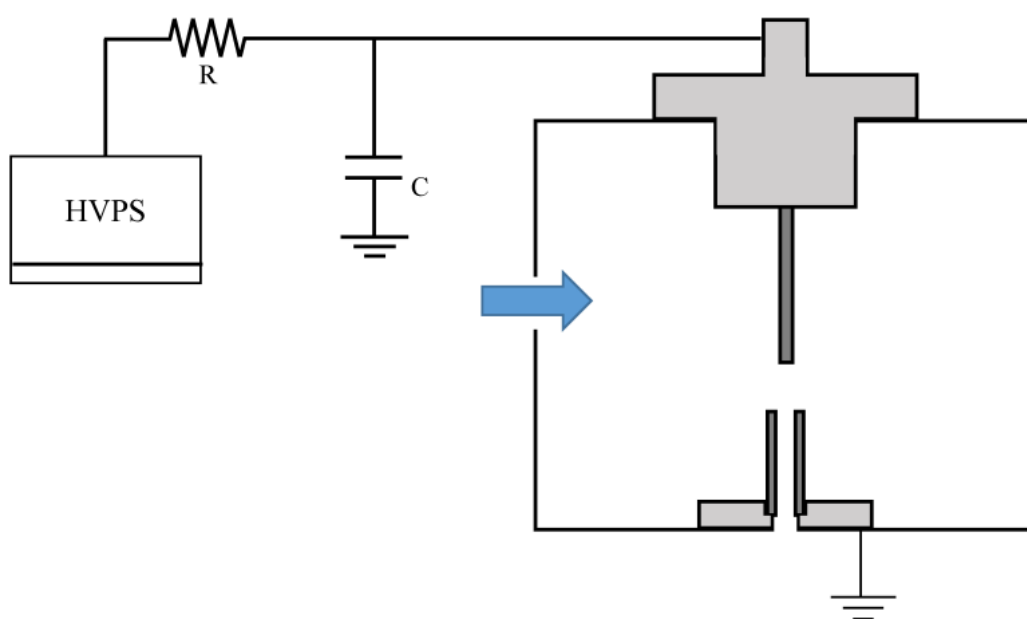


Figure 4.1. Schematic of spark discharge nanoparticle generation system which consist of external circuit and spark discharge chamber (blue arrow indicate carrier gas inflow)

4.2.2. Measurement system

The measurement system in this chapter was the same construction as used in chapter 3.

For voltage profile measurement, an oscilloscope (Agilent DSO-X 3014 A) equipped with a high voltage probe (Tektronix P6015A) was connected to the anode and then the spark discharge voltage and frequency of spark discharge was obtained.

The particle size distribution measurement system consists of a differential mobility analyzer (DMA, TSI 3085), a DMA controller (TSI 3776), and a condensation particle counter (CPC TSI 3776). The DMA scanned the nanoparticle size from 1 nm to 30 nm. And CPC counted the classified nanoparticles for obtaining the particle size distribution.

The measurements of particle size distribution have been conducted at an interval of 2 hours. At each measurement, the electrode gap size was adjusted to set the spark discharge voltage value to 2.6 kV by pushing the wire electrode into the spark discharge chamber.

4.3. Results and discussion

4.3.1. Consideration of cylinder wall thickness

The purpose of the wire-to-cylinder type electrode is to generate less agglomerated nanoparticles in high spark frequency regime with long term durability. To this end, the inner diameter of the cylinder has to be maintained in similar size for the confinement of the spark zone into the fast carrier gas flow field during spark discharge operation. The geometry of the electrode has been changed with spark discharge operation because the spark discharge erodes the electrode material. From this point of view, the smaller cylinder wall thickness is proper for the long term durability of nanoparticle generation. However, the wall thickness of the cylinder is involved in the capacity for the total amount of nanoparticle generation because the nanoparticles come from the electrode material. Therefore, proper thickness should be considered for efficient nanoparticle generation with long-term durability. In the previous study of the erosion pattern at the electrode after spark discharge operation (Wagner et al 2016), as seen in figure 4.2, erosion patterns of the electrode by spark discharge were shown uniformly on the surface of the electrode in the case of the rod-to-rod type electrode spark discharger. Moreover, in figure 4.3, each spark discharge left the circular patterns with 150 μm diameter approximately. Therefore, it is appropriate that the thickness of the cylinder should be designed to above the 150 μm for efficient nanoparticle generation by sufficient electrode

material erosion.

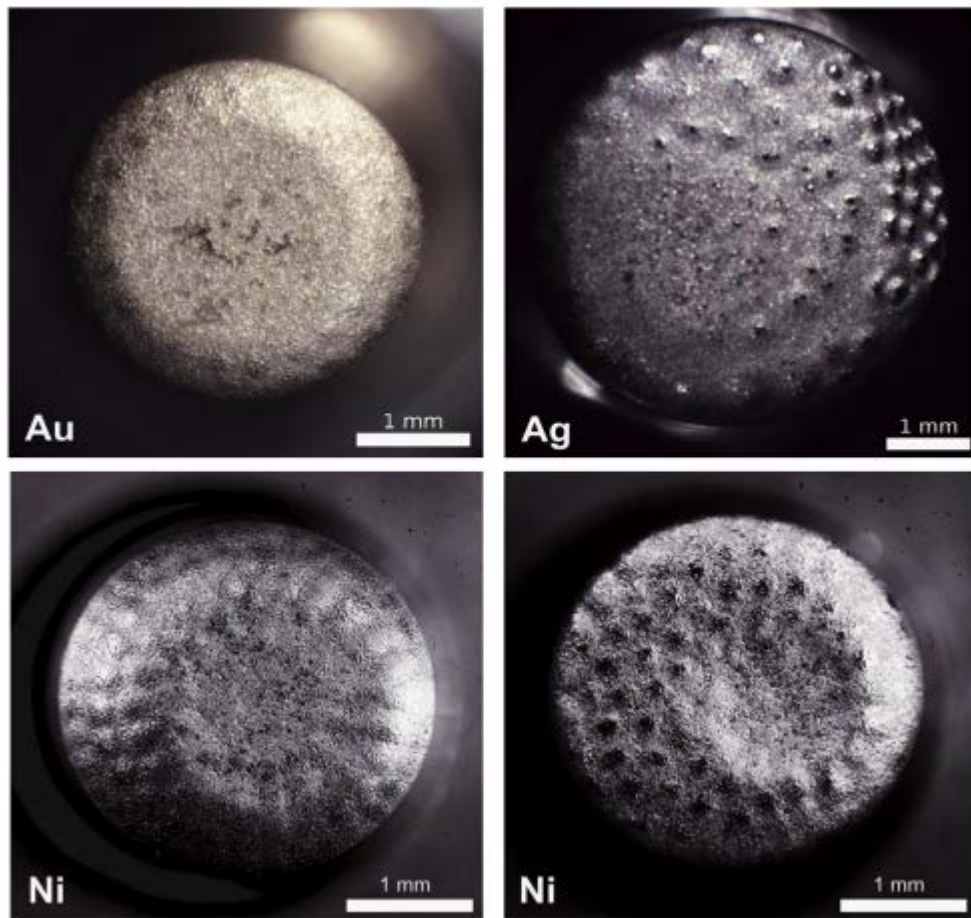


Figure 4.2. Optical images of spark electrode front surface (rod type) after spark discharge erosion. (Adopted from M. Wagner et al. 2016)

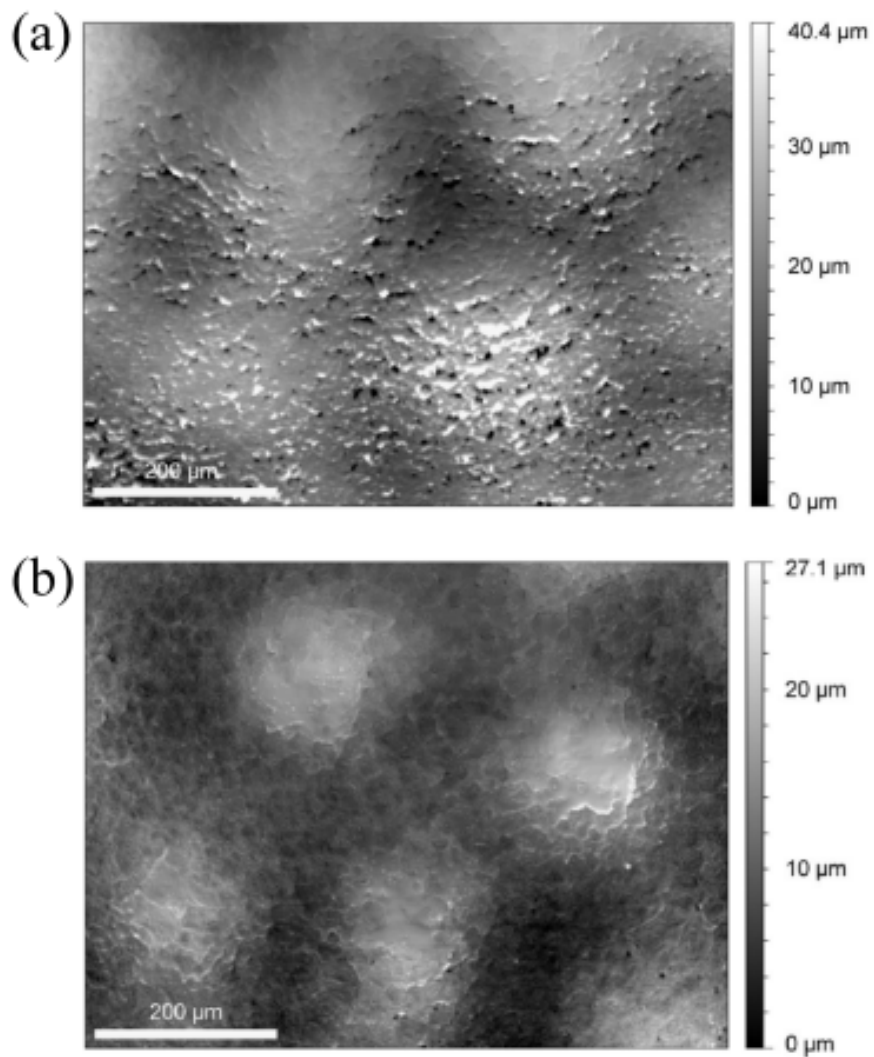


Figure 4.3. Confocal laser scanning height maps of patterns found on Ni electrode front surfaces of initially cathodic (a) and anodic polarity after spark discharge erosion. (Adopted from M. Wagner et al. 2016)

4.3.2. Electric field analysis for sustainable spark discharge

Each spark discharge vaporized the electrode material. And then, the flow field caused dilution and cooling of the vapor plume of electrode material. The rod-to-rod type electrode spark discharger could generate nanoparticles with long-term consistent size distribution due to the similar flow field in the whole spark zone between electrodes. Therefore, the spark discharge in the vicinity of similar flow field during spark operation is important condition for long-term consistent nanoparticle generation.

Unlike the case of the rod-to-rod electrode, the wire-to-cylinder type electrode spark discharger had asymmetric flow field where the flow rate was fast only in vicinity of the cylinder upper outlet. Therefore, it was important to keep the spark discharge consistent into the similar flow field site of the cylinder upper outlet.

To keep the spark discharge zone consistent during long-term spark discharge operation, the electric field simulation with COMSOL has been conducted with varying thickness of cylinder electrodes. The inner volume of the spark discharge chamber was modelled as seen in figure 4.4. The gap size between electrodes, the inner diameter of the cylinder electrode and the electric potential applied to the wire electrode were set to 1 mm, 1.6 mm, 1 kV, respectively in all cases. The cylinder electrode and cylinder holder were grounded.

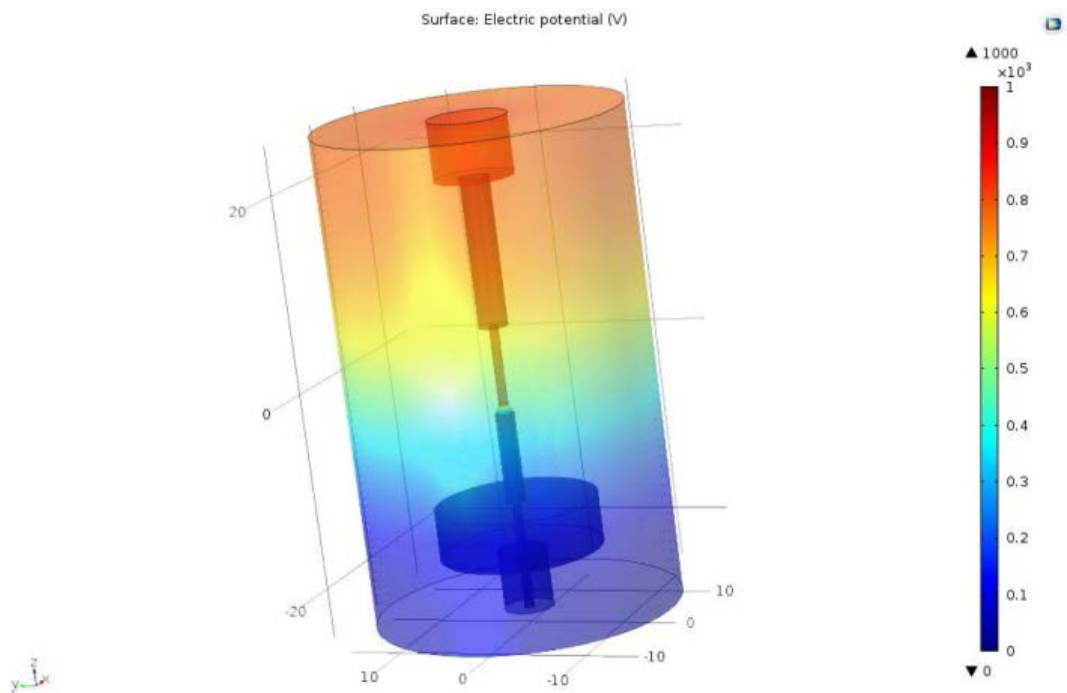


Figure 4.4. The COMSOL modelling of inner volume of spark discharge chamber with wire-to-cylinder type electrode (1mm diameter of wire, 0.2 mm thickness of cylinder wall case)

The electric field normalization values between electrodes were obtained with different thicknesses of the cylinder wall as seen in figure 4.5. The electrical breakdown of carrier gas occurred along the path which developed the strongest electric field. Therefore, two possible paths from the edge of the wire electrode to the inner and outer edge of the cylinder electrode were compared for finding the path of spark discharge. In the case of the cylinder wall thickness of 1 mm (figure 4.5(a)), the electric field normalization plot along the path 1 was higher than that along the path 2. It means that the spark discharge occurred from the wire to the inner edge of the cylinder electrode at first. After the erosion of the inner edge of the cylinder electrode, the spark discharge developed outward to select the strongest electric field. And it hindered the long-term consistent nanoparticle generation due to the change of spark zone toward slower carrier gas flow field. However, as the thickness of cylinder electrodes decreased (figure 4.5(b), (c)), the electric fields toward the inner edge and the outer edge of the cylinder electrode became similar. It means that the spark discharge might be confined into the upper cross section of the cylinder electrode uniformly such that the nanoparticle could be generated in the same flow velocity field. As a result, long-term consistent nanoparticle generation could be achieved because the spark zone was confined to the same carrier gas flow field.

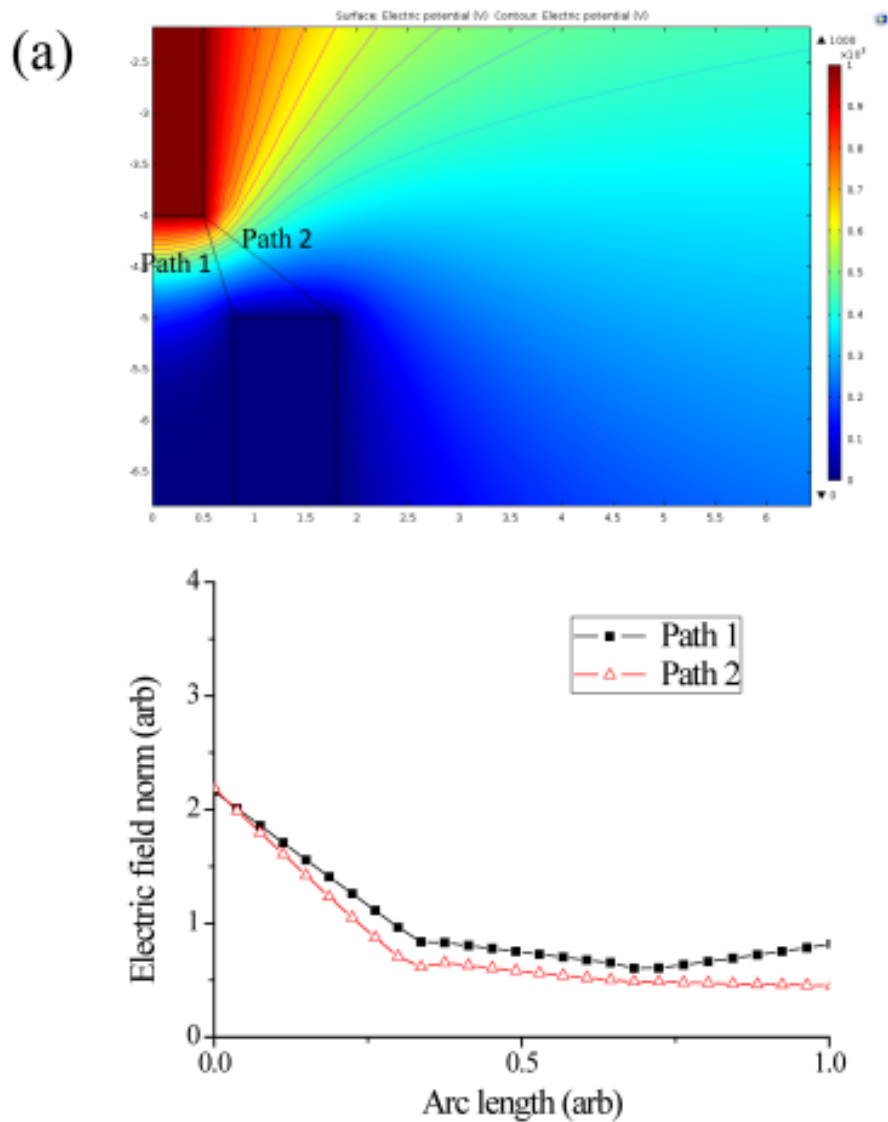


Figure 4.5. (a) Electric potential between electrodes (upper) and electric field normalization value along the path 1 and 2 when using the cylinder wall thickness of 1 mm.

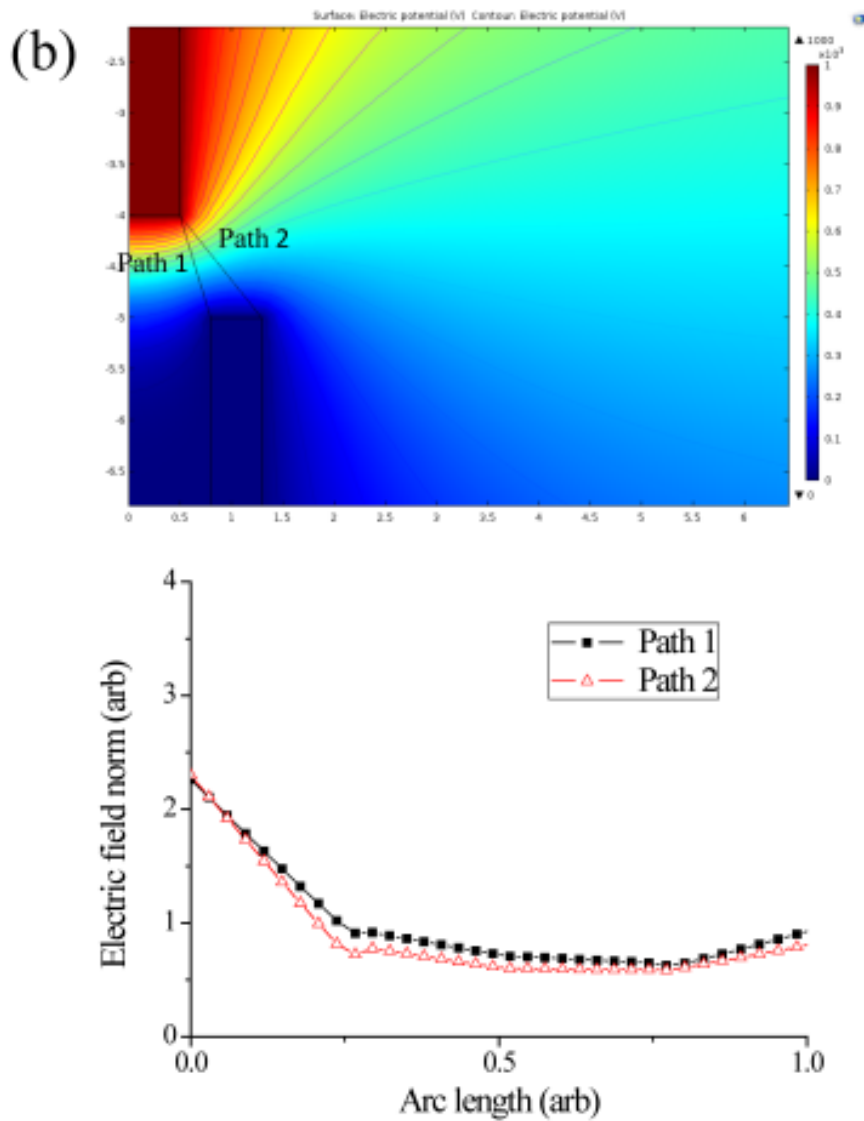


Figure 4.5. (b) Electric potential between electrodes (upper) and electric field normalization value along the path 1 and 2 when using the cylinder wall thickness of 0.5 mm.

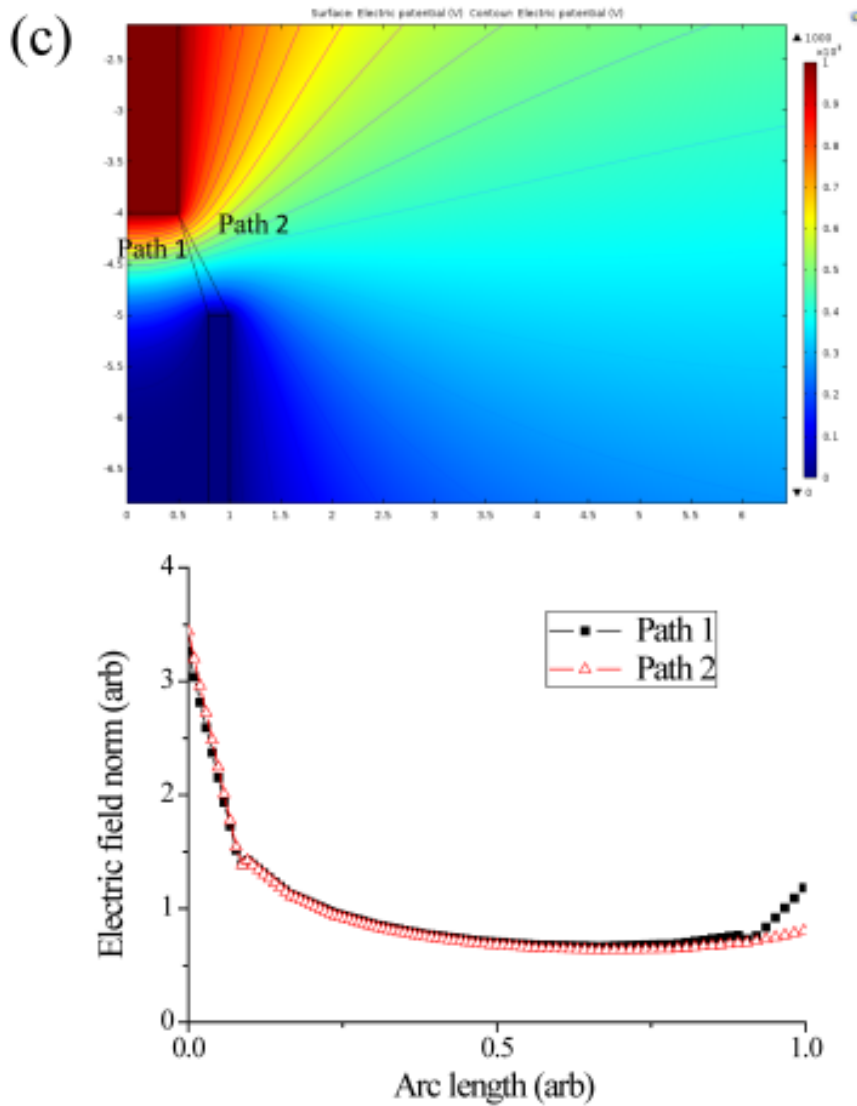


Figure 4.5. (c) Electric potential between electrodes (upper) and electric field normalization value along the path 1 and 2 when using the cylinder wall thickness of 0.2 mm.

4.3.3. Durability enhancement of Wire-to-cylinder type electrode

We confirmed the long-term durability of nanoparticle generation by using the wire-to-cylinder type electrode spark discharger. The cylinder electrode of 0.2 mm thickness was utilized in this study for uniform spark discharges on the upper cross section of the cylinder electrode. The external capacitance was set to 2 nF. The spark discharge voltage was set to 2.6 kV by adjusting the gap size of electrodes at each measurement. In figure 4.6 and 4.7, we confirmed that the wire-to-cylinder type spark discharger could generate nanoparticles in similar size distribution for 14 hours of spark operation with different frequencies. Total number concentration, geometric mean diameter and geometric standard deviation were also kept similar values for 14 hours. In the wire-to-cylinder type spark discharger, it was noted that the electrode geometry at spark discharge zone was kept regardless of erosion by spark discharge operation. Therefore, long-term durability of nanoparticle generation was attributed to the confinement of the spark zone within the same carrier gas flow field.

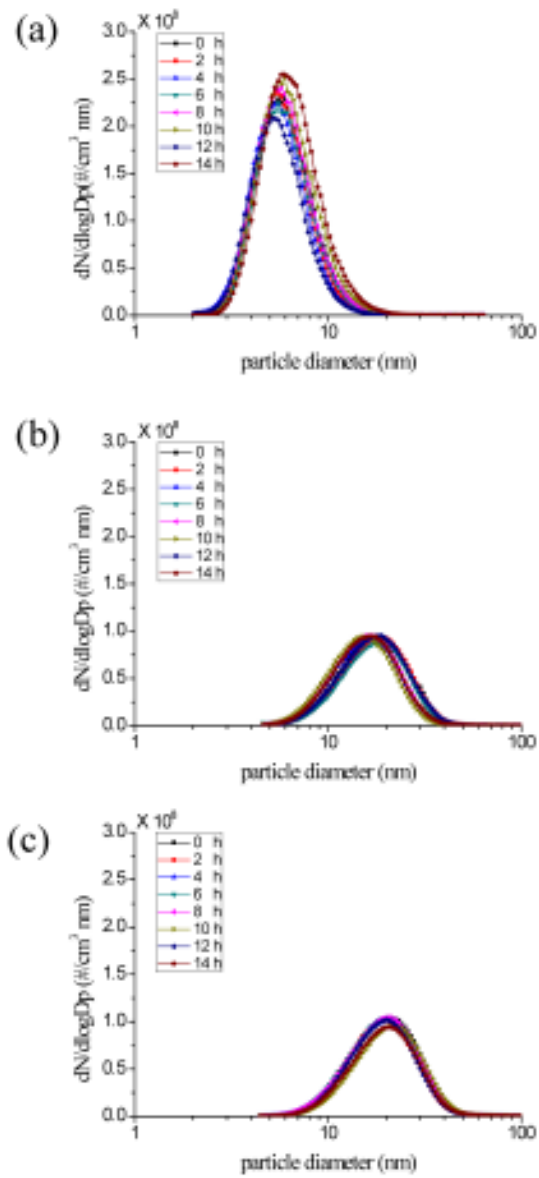


Figure 4.6. Long-term stability of nanoparticle size distribution with frequency of (a) 1.5 kHz (b) 3 kHz (c) 5 kHz by using wire (1mm diameter) -to-cylinder (1.6 mm inner diameter, 0.2 mm thickness) type electrode spark discharger.

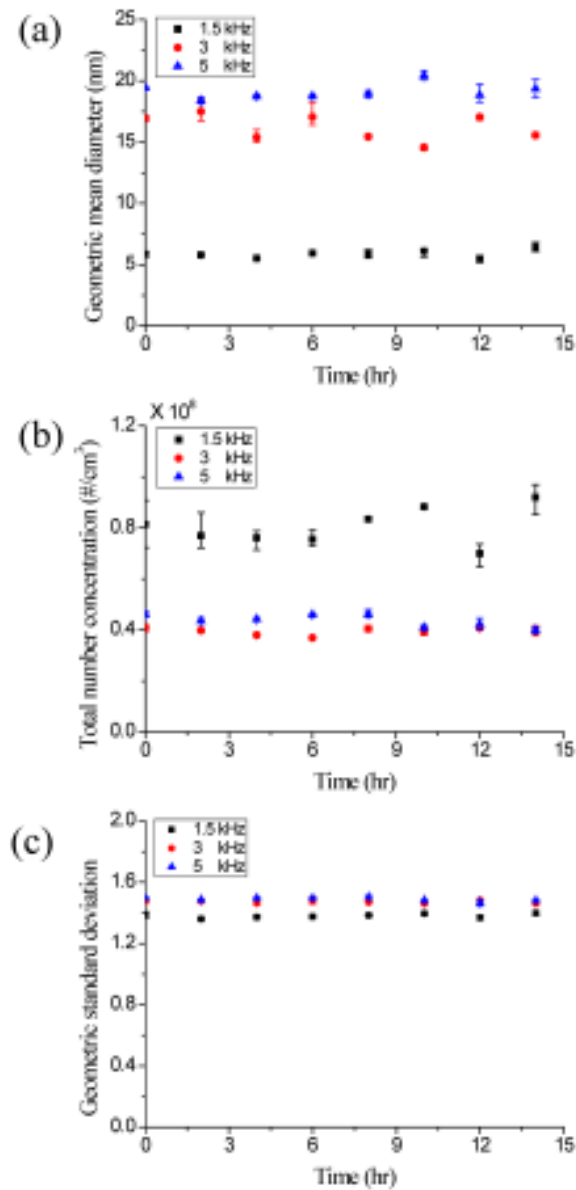


Figure 4.7. Long-term stability of (a) geometric mean diameter, (b) total number concentration and (c) geometric standard deviation with different frequencies by using wire (1mm diameter) -to-cylinder (1.6 mm inner diameter, 0.2 mm thickness) type electrode spark discharger.

4.4. Conclusion

We have developed a wire-to-cylinder type spark discharger that enables the long-term consistent nanoparticle generation. For determining the wall thickness of cylinder electrode, the erosion patterns of electrode by spark discharges were studied. The erosion patterns were shown in the circular forms with a diameter of 150 μm , which were distributed on the surface of electrodes. And it means that the thickness of the cylinder wall has to be greater than this spark pattern size for efficient vapor generation. The COMSOL electric field simulation was also conducted for finding the proper thickness of the cylinder electrode. In electric field simulation, as the thickness of the cylinder electrode decreased, spark discharge developed uniformly at the upper cross section of the cylinder electrode. Lastly, we confirmed that the wire-to-cylinder (wall thickness = 0.2 mm) type spark discharger could generate nanoparticles with consistent size distribution for 14 hours.

Chapter 5.

Concluding Remarks

In this study, we devised a new spark discharge scheme to increase the production of positively charged particles by using the electrodes themselves of the spark discharger as the supplier of positive ions in situ. And we investigated the factors which affect the stability of spark discharge in high frequency region. Finally, we invented the wire-to-cylinder type electrode for consistent generation of nanoparticles with high frequency.

To this end, in chapter 2, we invented a new spark control circuit to maintain the voltage of the electrode with the value above the corona discharge voltage, always excepting the moment of spark discharge. We confirmed the 1.8-fold increase of the amount of positively charged particles generated from the spark discharger when using the pin-to-plate type electrodes and the new circuit. And the amount of the negatively charged particles was reduced by half due to the increase of positive ion generation. For investigating the effects of the electrode geometry, we conducted the comparative study on generation of positively charged particles between rod-to-plate and wire-in-hole type electrodes.

In chapter 3, for understanding the effect of electrode geometry on the stability of spark discharge, we conducted comparative study between the wire-to-plate electrode type and the rod-to-rod spark discharger. With using the rod-to-rod type electrode configuration, the spark discharge voltage dropped to the voltage below the desired break down voltage of the spark discharger (unstable state) over the spark frequency of 1.1 kHz. On the other hand, the spark discharge voltage was

maintained as the desired break down voltage (stable state) of the spark discharger with the wire-to-plate electrode configuration over the spark frequency of 10 kHz.

In the wire-to-plate electrode type spark discharger, the carrier gas velocity in vicinity of spark discharge is much faster than that in the rod-to-rod electrode type spark discharger. In addition, we confirmed the stable state of spark discharge with the wire-to-plate electrode type spark discharger changed to unstable state due to the decrease in the carrier gas flow rate. Therefore, we identified that the carrier gas velocity in vicinity of spark discharge was a main factor for maintaining stable condition of spark dischargers over the frequency of 10 kHz. Moreover, we investigated the effect of the electric field near the spark discharge zone on the stability of spark discharge. To this end, we measured the spark stability of the wire-to-rod type electrode. Its carrier gas velocity field has a similarity to that of the rod-to-rod type electrode but the wire-to-rod type electrode can develop stronger electric field intensity due to the wire electrode. Then, we confirmed that the wire-to-plate type electrode could maintain the stable state over the frequency in which the rod-to-rod type electrode exhibited unstable state.

Finally, in chapter 4, we invented the wire-to-cylinder type electrode for time-consistent and stable spark discharge generation. We determined the proper thickness of cylinder electrode by using COMSOL simulation of electric field. We confirmed the long term stability of spark discharge above 1 kHz.

References

- Adachi, M., Kousaka, Y., & Okuyama, K. (1985). Unipolar and bipolar diffusion charging of ultrafine aerosol particles. *Journal of Aerosol Science*, 16(2), 109-123.
- Alonso, M., Martin, M. I., & Alguacil, F. J. (2006). The measurement of charging efficiencies and losses of aerosol nanoparticles in a corona charger. *Journal of Electrostatics*, 64(3-4), 203-214.
- Bau, S., Witschger, O., Gensdarmes, F., Thomas, D., & Borra, J. P. (2010). Electrical properties of airborne nanoparticles produced by a commercial spark-discharge generator. *Journal of Nanoparticle Research*, 12(6), 1989-1995.
- Borra, J.-P. (2006). Nucleation and aerosol processing in atmospheric pressure electrical discharges: powders production, coatings and filtration. *Journal of Physics D: Applied Physics* 39:R19.
- Chae, S., Lee, D., Kim, M.-C., Kim, D. S., & Choi, M. (2015). Wire-in-Hole-Type Spark Discharge Generator for Long-Time Consistent Generation of Unagglomerated Nanoparticles. *Aerosol Science and Technology*, 49(7),

463-471.

Efimov, A. A., Ivanov V, V., Bagazeev, A, V., Beketov, I, V., Volkov, I, A., Shcherbinin, S, V. (2013). Generation of Aerosol Nanoparticles by Multi-Spark Discharge Generator. *Technical Physics Letter* 39:053-1056.

Efimov, A, A., Lizunova, A, A., Volkov, I, A., Mylnikov, D, A., Arsenov P, V., Ivanov V, V. (2016). A new approach to the high-yield synthesis of nanoparticles by spark discharge. *Journal of Physics: Conference Series* 741:012035.

Evans, D. E., Jarrison, R. M., and Ayres, J. G. (2003). The Generation and Characterisation of Elemental Carbon Aerosols for Human Challenge Studies. *Journal of Aerosol Science.*, 34:23-1041.

Ha, K., Choi, H., Jung, K., Han, K., Lee, J, K., Ahn, K., Choi, M.(2014). Large-area assembly of three-dimensional nanoparticle structures via ion assisted aerosol lithography with a multi-pin spark discharge generator. *Nanotechnology* 25:225302.

Ha, K., Jang, E., Jang, S., Lee, J.-K., Jang, M. S., Choi, H., Cho, J.-S., Choi, M.

(2016). A light-trapping strategy for nanocrystalline silicon thin-film solar cells using three-dimensionally assembled nanoparticle structures. *Nanotechnology* 27:055403.

Han, K., Kim, W., Yu, J., Lee, J., Lee, H., Woo, C. G., & Choi, M. (2012). A study of pin-to-plate type spark discharge generator for producing unagglomerated nanoaerosols. *Journal of Aerosol Science*, 52, 80-88.

Hinds, W. C. (1999). *Aerosol technology: properties, behavior, and measurement of airborne particles*(2nd ed.): John Wiley & Sons, (Chapter 15).

Horvath, H., and Gangl, M. (2003). A Low-Voltage Spark Generator for Production of Carbon Particles. *Journal of Aerosol Science.*, 34:581-1588.

Jung, K., Hahn, J., In, S., Bae, Y., Lee, H., Pikhitsa, P. V., Ahn, K., Ha, K., Lee, J. K., Park, N., Choi, M. (2014). Hotspot-Engineered 3D Multipetal Flower Assemblies for Surface-Enhanced Raman Spectroscopy. *Advanced Materials* 26:5924-5929.

Jang, S., Yoon, J., Ha, K., Kim, M.-c., Kim, D. H., Kim, S. M., Kang, S. M., Park, S. J., Jung, H. S., Choi, M. (2016). Facile fabrication of three-dimensional

TiO₂ structures for highly efficient perovskite solar cells. *Nano Energy* 22:499-506.

Kim, M.-c., Kim, B. J., Yoon, J., Lee, J.-w., Suh, D., Park, N.-g., Choi, M., Jung, H. S. (2015). Electro-spray deposition of a mesoporous TiO₂ charge collection layer: toward large scale and continuous production of high efficiency perovskite solar cells. *Nanoscale* 7:20725-20733.

Lee, H., You, S., Pikhitsa, P. V., Kim, J., Kwon, S., Woo, C. G., Choi, M. (2010). Three-dimensional assembly of nanoparticles from charged aerosols. *Nano letters* 11:119-124.

Meek, J. M. (1940). A Theory of Spark Discharge. *Physical Review*, 57(8), 722-728.

Messing, M. E., Dick, K. A., Wallenberg, L. R., & Deppert, K. (2009). Generation of size-selected gold nanoparticles by spark discharge—for growth of epitaxial nanowires. *Gold Bulletin*, 42(1), 20-26.

Meuller, B. O., Messing, M. E., Engberg, D. L., Jansson, A. M., Johansson, L. I., Norlén, S. M., Tureson, N., Deppert, K. (2012). Review of spark discharge

generators for production of nanoparticle aerosols. *Aerosol Science and Technology* 46:1256-1270.

Park, K. T., Farid, M. M., & Hwang, J. (2014). Anti-agglomeration of spark discharge-generated aerosols via unipolar air ions. *Journal of Aerosol Science*, 67, 144-156.

Pfeiffer, T., Feng, J., Schmidt-Ott, A. (2014). New developments in spark production of nanoparticles. *Advanced Powder Technology* 25:56-70.

Schwyn, S., Garwin, E., Schmidt-Ott, A. (1988). Aerosol generation by spark discharge. *Journal of Aerosol Science* 19:639-642.

Sung, H., Lee, J., Han, K., Lee, J.-K., Sung, J., Kim, D., Choi, M., & Kim, C. (2014). Controlled positioning of metal nanoparticles in an organic light-emitting device for enhanced quantum efficiency. *Organic Electronics*, 15(2), 491-499.

Tablizi, N. S., Ullmann, M., Vons, V. A., Lafont, U., and Schmidt-Ott, A. (2009). Generation of Nanoparticles by Spark Discharge. *Journal of Nanoparticle Research.*, 11:315-332.

Wagner M., Kohut A., Geretovszky Z., Seipenbusch M., Galbacs G. (2016).
Observation of fine-ordered patterns on electrode surfaces subjected to
extensive erosion in a spark discharge. *Journal of Aerosol Science* 93, 16-
20.

국문 초록

내부 나노입자 생산량 향상을 위한 단일 스파크 방전 장치 개선 연구

서울대학교 대학원 기계항공공학부

노 승 렬

나노입자는 그 고유의 광학, 촉매, 전기적 특성 등으로 인하여 많은 분야에 사용 되고 있다. 나노입자를 생산하는 여러 방법 중, 스파크 방전을 이용한 나노입자 생산법은 방법의 편의성, 경제성, 생산된 나노입자의 순수성이 여타의 다른 방법에 비하여 뛰어나기 때문에, 많은 연구가 진행 되어 오고 있는 분야이다. 특히, 스파크 방전을 이용하여 발생된 나노입자는 그 중 일부가 공기 중의 하전된 형태로 존재한다는 장점이 있기 때문에, 에어로졸 기반의 정전기적 패터닝의 주된 재료로 사용되고 있다. 따라서 본 연구는, 스파크 방전 장치의

개선을 통하여, 스파크 방전을 통하여 발생한 나노입자의 생산 효율 및 생산량을 증가시키는데 그 목표를 갖고 진행하였다.

이를 위하여 스파크 방전 나노입자 발생 장치의 구성 요소 중, 스파크 방전 외부 회로를 변형 시켜, 하전 입자량 생산의 증가를 얻어내었다. 변형된 외부 회로에서는, 기존의 회로에 추가 전압공급장치와 저항을 병렬로 연결하여 스파크 방전 사이에 코로나 방전이 발생하도록 하였으며, 이를 통하여 양하전 입자량을 최대 약 80 퍼센트 증가 시킬 수 있었다. 또한, 코로나 방전이 일어나지 않는 스파크 전극을 사용한 비교 실험을 통하여, 본 회로가 코로나 방전을 통하여 하전된 나노입자 생산량 증가에 도움을 주고 있음을 밝혀 내었다.

또한, 본 연구에서는 나노입자 생산량 증가를 위한 방법 중 하나인, 스파크 방전 주파수를 늘리는 방법에 필요한 실험 변수들을 찾는 연구도 진행하였다. 기존의 봉-봉 구조의 스파크 방전 장치에서는 1kHz 이상의 스파크 방전 주파수를 얻어 낼 수 없었으나, 본 연구에서는 봉-판 구조, 와이어-판 구조의 스파크 방전 장치와의 비교 실험을 통하여, 고주파의 스파크 방전을 얻기 위해서는 스파크 방전 부분의 강한 전기장의 세기와 기체 유속의 증가가 필요하다는 사실을 밝혀 내었다.

위의 연구를 통하여, 실제 산업 현장에 적용 가능한 고주파 스파크 방전 장치의 전극 구조인 와이어-원통 구조를 개발하였으며,

시뮬레이션과 사전 연구를 토대로, 원통의 두께 및 와이어의 두께의 적합한 값에 대한 연구를 진행하였다. 또한, 이 전극 구조를 사용하여, 장시간의 고주파 스파크 방전에도 비슷한 나노입자 크기 분포를 얻을 수 있음을 확인하였다.

주요어: 스파크 방전 회로, 하전 나노입자, 생산량 증가, 고주파 스파크 방전, 스파크 방전 전극

학번: 2010-20672